ARTICLE

Check for updates

Highly unstable heterogeneous representations in VIP interneurons of the anterior cingulate cortex

Connor Johnson[1,13], Lisa N. Kretsge[2,3,13], William W. Yen[1,13], Balaji Sriram[4], Alexandra O'Connor[5], Ruichen Sky Liu[6], Jessica C. Jimenez[7], Rhushikesh A. Phadke[8], Kelly K. Wingfield[3,9], Charlotte Yeung[1], Tushare J. Jinadasa[1], Thanh P. H. Nguyen[5], Eun Seon Cho[1], Erelle Fuchs[1], Eli D. Spevack[1], Berta Escude Velasco[1], Frances S. Hausmann[1], Luke A. Fournier[1], Alison Brack[8], Sarah Melzer[10] and Alberto Cruz-Martín[1,3,8,11,12]✉

A hallmark of the anterior cingulate cortex (ACC) is its functional heterogeneity. Functional and imaging studies revealed its importance in the encoding of anxiety-related and social stimuli, but it is unknown how microcircuits within the ACC encode these distinct stimuli. One type of inhibitory interneuron, which is positive for vasoactive intestinal peptide (VIP), is known to modulate the activity of pyramidal cells in local microcircuits, but it is unknown whether VIP cells in the ACC (VIP^{ACC}) are engaged by particular contexts or stimuli. Additionally, recent studies demonstrated that neuronal representations in other cortical areas can change over time at the level of the individual neuron. However, it is not known whether stimulus representations in the ACC remain stable over time. Using in vivo Ca^{2+} imaging and miniscopes in freely behaving mice to monitor neuronal activity with cellular resolution, we identified individual VIP^{ACC} that preferentially activated to distinct stimuli across diverse tasks. Importantly, although the population-level activity of the VIP^{ACC} remained stable across trials, the stimulus-selectivity of individual interneurons changed rapidly. These findings demonstrate marked functional heterogeneity and instability within interneuron populations in the ACC. This work contributes to our understanding of how the cortex encodes information across diverse contexts and provides insight into the complexity of neural processes involved in anxiety and social behavior.

Molecular Psychiatry; https://doi.org/10.1038/s41380-022-01485-y

INTRODUCTION

Cortical subregions are often implicated in a variety of behavioral functions, but it is not well understood how these areas encode such diverse information. The anterior cingulate cortex (ACC) is necessary for emotional processing and social cognition, but how it encodes stimuli relevant to both processes is unknown [1–6]. In humans, ACC activity increases when healthy subjects perform social tasks and is higher in anxiety disorder patients who demonstrate increased symptom severity [7]. In rodents and non-human primates, ACC inhibition via lesions or genetic manipulations impairs social behaviors [8–10]. In addition, stimulating activity or silencing a cytoskeletal protein in the rodent ACC alters anxiety-like behaviors [11, 12]. Recent studies in rodents have provided insight into the ACC's importance in emotional and social behaviors by monitoring either single unit or bulk activity of this region [6, 8, 11, 13–16]. However, these data do not parse out the roles of different neural subtypes or microcircuits within the ACC. It remains unknown how neuronal representations of diverse stimuli are embedded within ACC subcircuits.

Inhibitory neurons that are positive for vasoactive intestinal peptide (VIP) often inhibit other inhibitory cells, thereby driving excitatory pyramidal (Pyr) cell activity [17–19]. VIP cells, therefore, are in a unique position to modulate local activity [20–22]. This interneuron type also receives long-range inputs, which may allow them to coordinate the activity of the ACC by integrating the inputs from brain regions that respond to diverse stimuli [18, 23]. Acetylcholine, serotonin, and gastrin-releasing peptide can modulate functionally distinct groups of VIP interneurons and may differentially engage them during various behaviors [22, 24–26]. Additionally, a subclass of VIP cell can directly excite neighboring neurons through fast synaptic transmission of acetylcholine [27], although these cells were subsequently found to be very rare [28]. VIP cells in the visual cortex activate differently to novel stimuli compared to familiar stimuli and, in the auditory cortex, to novel sounds and shocks during fear conditioning [22, 29]. Additionally, hippocampal VIP interneurons form functional clusters that are differently modulated by behavioral states [30]. Although a previous study imaged VIP cells with cellular

[1]Neurobiology Section in the Department of Biology, Boston University, Boston, MA, USA. [2]The Graduate Program for Neuroscience, Boston University, Boston, MA, USA. [3]Neurophotonics Center, Boston University, Boston, MA, USA. [4]Praxis Precision Medicines, Inc., Boston, MA, USA. [5]Department of Biomedical Engineering, Boston University, Boston, MA, USA. [6]MS in Statistical Practice Program, Boston University, Boston, MA, USA. [7]Department of Neurology, University of California, San Francisco, San Francisco, CA, USA. [8]Molecular Biology, Cell Biology and Biochemistry Program, Boston University, Boston, MA, USA. [9]Department of Pharmacology and Experimental Therapeutics, Boston University, Boston, MA, USA. [10]Department of Neurobiology, Howard Hughes Medical Institute, Harvard Medical School, Boston, MA, USA. [11]Center for Systems Neuroscience, Boston University, Boston, MA, USA. [12]The Center for Network Systems Biology, Boston University, Boston, MA, USA. [13]These authors contributed equally: Connor Johnson, Lisa N. Kretsge, William W. Yen. ✉email: martini.cruz@gmail.com

Received: 5 February 2021 Revised: 7 February 2022 Accepted: 9 February 2022
Published online: 04 March 2022

resolution in the prefrontal cortex (PFC), it did not extensively explore the functional heterogeneity of this interneuron type [31]. Despite the varied molecular, morphological, and electrophysiological properties of VIP cells [32–35], little is known about the functional diversity of VIP interneurons in the ACC (VIP^{ACC}) and no existing studies have used single-cell resolution imaging techniques in vivo to investigate this.

Recently, several studies have shown that behavior and population-level neural dynamics can remain stable over time, even when individual Pyr cells that are engaged by those stimuli demonstrate dramatic changes in their activity patterns [36–40]. This has been hypothesized to be an adaptive feature of neural function that is important for learning and memory, and efficient coding [38, 41]. In the avian brain, interneuron activity remained stable even when projection neurons coding for song changed from day to day [36]. However, in the mammalian cortex not much is known about the dynamics of interneuronal representations.

Using miniscopes [42], we performed in vivo single-cell resolution Ca^{2+} imaging of VIP^{ACC} to investigate their functional heterogeneity and stability across tasks that assay different behavioral modalities. We identified individual VIP^{ACC} that preferentially activated to anxiety-related, social, or non-social stimuli. When the same neurons were monitored across multiple trials, stimulus-selective encoding of individual neurons was highly unstable over time. This effect was consistent across a range of tasks and time scales. Overall, our data show that VIP^{ACC} are functionally heterogeneous and their encoding is highly unstable, providing a new framework to better understand how VIP cells encode diverse stimuli in the ACC.

MATERIALS AND METHODS

Animals

Animals were group-housed in a 12-h light/dark schedule vivarium with food and water ad libitum. Experimental mice for Ca^{2+} imaging experiments were male postnatal day (P) 60–120 VIP-Cre mice [43] (Vip-IRES-Cre, #010908, The Jackson Laboratory, Bar Harbor, Maine, RRID: IMSR_JAX:010908). Stimulus mice for social interaction were littermates (male VIP-Cre) or novel (age and sex matched male CD-1 IGS, strain code: 022, Charles River Laboratories, Wilmington, Massachusetts). Non-implanted controls for behavior were also male P60-120 VIP-Cre mice. For c-Fos experiments, male and female P60-120 VIP-Cre mice were used. For rabies tracing experiments, male P60-120 SST-Cre [43] (SST-IRES-Cre, #013044, The Jackson Laboratory, Bar Harbor, Maine) and PV-Cre [44] (B6 PV^{Cre}, #017320, The Jackson Laboratory, Bar Harbor, Maine) mice were used in addition to VIP-Cre mice. For electrophysiology experiments, we generated mice expressing EGFP in the nuclei of VIP cells (VIP-Cre x H2B-EGFP) by crossing VIP-Cre mice with the strain B6;129S4-Gt(ROSA)$^{26Sortm2(CAG-HIST1H2BB/EGFP)Zjh}$/J [45] (IMSR Cat# JAX:028581, The Jackson Laboratory, Bar Harbor, Maine, RRID:IMSR_JAX:028581). These mice received viral injections at 6–10 weeks and were used for electrophysiology at least three weeks later. Wild type mice (C57BL/6 J, #000664, The Jackson Laboratory, Bar Harbor, Maine) were used for control virus injections. All procedures were approved by the Institutional Animal Care and Use Committee (IACUC) at Boston University and practices were consistent with the Guide for the Care and Use of Laboratory Animals and the Animal Welfare Act.

Surgeries

Surgeries were performed using aseptic surgical techniques with autoclaved instruments. Animals were weighed and subsequently induced in a chamber with an isoflurane–oxygen mixture (4% (v/v), Henry Schein, Melville, New York). Anesthesia was maintained throughout the procedure via mask inhalation of an isoflurane–oxygen mixture (1–1.5% (v/v)). Animals were kept on a heating pad (T Pump, Gaymar Industries Inc., Orchard Park, New York) for the duration of the surgeries and for 30-min recovery periods before being returned to their home cages. Animals were injected with buprenorphine (3.25 mg/kg; SC, Patterson Veterinary, Greeley, Colorado), meloxicam (5 mg/kg; SC, Covetrus, Dublin, Ohio), and dexamethasone (2.5 mg/kg; SC, Henry Schein, Melville, New York) and the fur on the top of the head was removed. Animals were head-fixed using a stereotax (Kopf Instruments, Tujunga, California). The surgical area was sterilized with 10% povidone-iodine and 70% isopropyl alcohol (CVS, Woonsocket, Rhode Island) and local anesthetic was applied (lidocaine 1% and epinephrine, 1:100,000; SC, Henry Schein, Melville, New York). After surgeries, post-operative analgesics were administered for 2 days, twice per day (buprenorphine, 0.01 mg/kg; SC and meloxicam, 5 mg/kg; SC, Henry Schein, Melville, New York).

Viral injections. After the preparations above, an incision was made in the skin along the midline of the skull. A craniotomy was made over the injection site using a pneumatic dental drill. Using a stereotax and the Nanoject II (Drummond Scientific, Broomall, Pennsylvania), a pulled-glass pipette (BF150-117-10; tip size approximately 3–15 µm, Sutter Instrument Co., Novato, California) was lowered into the ACC (AP: + 0.90 mm, ML: −0.30 mm, DV: −1.00 mm) or retrosplenial cortex (RSC, AP: −3.0 mm, ML: 0.5 mm, DV: −0.6 mm) and virus was injected. After pipette removal, the skin was sutured with non-absorbable sutures (AD Surgical, Sunnyvale, California).

To monitor VIP^{ACC} activity, we injected the ACC with 460 nl of an adeno-associated virus (AAV) that expresses GCaMP6f, a genetically-encoded fluorescent Ca^{2+} indicator, in a Cre-dependent manner (AAV9-CAG-Flex-GCaMP6f.SV40, titer: 5.23×10^{13} GC/ml, packaged by the University of Pennsylvania Vector Core, Philadelphia, Pennsylvania). When these injections were performed in wild-type mice, they showed no GCaMP fluorescence ($N = 3$).

To fluorescently label VIP^{ACC} for c-Fos experiments, we injected the ACC with 460 nl of an AAV that expresses enhanced green fluorescent protein (EGFP) in a Cre-dependent manner (AAV1-CAG-Flex-EGFP.WPRE.bGH, titer: 1.00×10^{12} GC/ml, plasmid #65455, Addgene, Watertown, Massachusetts) [46].

For rabies trans-synaptic tracing, we used either VIP-Cre, SST-Cre, or PV-Cre mice and injected the ACC. For each animal, we first injected 128 nl of a helper AAV that expresses target proteins under the human synapsin-1 promoter: AAV2/1-synP-Flex-split-TVA-EGFP-B19G (AAV-TVA-Glyco) [47] (titer: 0.98×10^{12} GC/ml, University of North Carolina Viral Core, Chapel Hill, North Carolina). This AAV contained genes to express EGFP, the avian sarcoma/leukosis virus subtype A receptor (TVA, which confers infection capability to rabies virus pseudotyped with the avian sarcoma leucosis virus glycoprotein (EnvA)), and the rabies virus glycoprotein (G or Glyco) [47, 48] (which is necessary for trans-synaptic transport of glycoprotein gene-deleted (ΔG) rabies virus (RV)) [23]. These three genes were in frame and separated by porcine teschovirus self-cleaving 2 A elements [47]. After allowing the virus to express for one month, the skin was re-incised, a new craniotomy was drilled, and 128 nl of ΔG EnvA pseudotyped RV with mCherry was injected (EnvA-ΔG-mCherry, titer: 1.5×10^9 GC/ml, Boston's Children Hospital Viral Core, Boston, Massachusetts). There is no cognate receptor for EnvA in the mouse, so EnvA-ΔG-mCherry only infects TVA-expressing cells. Together, Glyco, TVA, and EnvA-ΔG-mCherry allow for retrograde monosynaptic tracing only from Cre-expressing cells. We performed these injections in wild type mice and saw no labeled cells outside of the injection site, suggesting a lack of leaky expression in the rest of the brain ($N = 3$).

To perform electrophysiology experiments with optogenetic manipulation, we injected two AAVs into the RSC of VIP-Cre x H2B-EGFP mice. Each animal was injected bilaterally with 300 nl of a solution containing both AAV2/9-hSyn-Cre-WPRE-hGH (titer: $1.1*10^{12}$ GC/ml, viral prep #105553-AAV9, Addgene, Watertown, Massachusetts; RRID:Addgene_105553) and AAV2/2-EF1a-DIO-hChR2(H134R)-mCherry-WPRE-pA (titer: $4*10^{12}$ GC/ml, University of North Carolina Viral Core, Chapel Hill, North Carolina). This approach allowed us to express ChR2-mCherry in RSC neurons and stimulate the axonal projections in the ACC.

GRIN lens implants. To image neuronal activity with a miniaturized microscope (miniscope), a gradient-index (GRIN) lens was implanted in the ACC at least 2 weeks after viral injection (to allow for maximal GCaMP6f expression). After the preparations above, the scalp was re-incised and a 1 mm diameter craniotomy was drilled, centered around the viral injection. Three screws (Fine Science Tools Inc., North Vancouver, Canada) were inserted into the skull and a layer of super glue (cyanoacrylate, Krazy glue, High Point, North Carolina) was applied to ensure the lens and dental cement adhered strongly. Dura over the ACC and a small region of the secondary motor cortex were aspirated using a blunted 18 G needle (BD, Franklin Lakes, NJ) coupled to a vacuum line. A GRIN lens (Table S1) attached to a stereotax via custom 3D-printed implant assembly (Fig. S1A-G) was lowered into the ACC at a 20° angle (AP: +0.90 mm, ML: −0.12 mm, DV: −0.13 mm) to improve access to the ACC and minimize the risk of

puncturing the midline vasculature. Lenses were adhered to the skull with optical glue (Norland Products Inc., Cranbury, NJ) and dental cement (Ortho-Jet™ Liquid, Black, Lang Dental, Wheeling, Illinois). An antibiotic was administered via the water supply (Biomox, 0.75 mgl/ml, Henry Schein, Melville, New York) for 10 days after surgery.

3D-printed miniscopes and baseplating

3 weeks after lens implant surgeries (to allow for recovery and optimal GCaMP6f expression), animals were anesthetized, as described above, and GCaMP6f expression was assessed by imaging the fluorescent signal using miniscopes. When GCaMP6f-positive neurons were visible, baseplates were attached to the skulls with dental cement using a custom 3D-printed baseplating assembly (Fig. S1). The miniscopes used were modified from two existing designs [42, 49] to allow them to detach from the baseplate (Fig. S1), which made it possible to co-house the animals without risking miniscope damage. Miniscopes weighed approximately 3.5 g and the wire attaching them to the acquisition board rested in a plastic loop hanging from the ceiling to minimize the weight on the animal's head. This allowed animals to freely move and behave normally (Fig. S1). Miniscopes were attached to baseplates at a 15–20 degree angle relative to the midline to align with the GRIN lenses (Fig. S1). Miniscope models are available at https://github.com/CruzMartinLab. Commercially available parts are listed in Table S1. Custom parts were 3D-printed (Form 3 Printer, Black Resin FLGPBK03, Formlabs, Somerville, Massachusetts) and assembled in-house (Fig. S1).

Behavioral assays and in vivo Ca^{2+} imaging

Before any behavioral testing, mice were handled for 10 min for 3 days to acclimate them to the experimenter. For anxiety-related assays, mice were not exposed to the arenas prior to testing, but for the social tasks, implanted mice were acclimated to the arena with empty cups for 10 min per day, for 2 days prior to the task. In addition, stimulus mice were acclimated to being housed in cups for 10 min on each of these days. Arenas were custom made from acrylic and HDPE (McMaster-Carr, Elmhurst, Illinois) and were cleaned with 70% ethanol between trials and animals. Behavior was recorded with a camera (C270 Webcam, Logitech, Lausanne, Switzerland) at 30 frames/sec under overhead lighting (200 lux, unless otherwise noted). After miniscopes were attached, animals were given 10 min to rest in an empty chamber before we started the experiments. Ca^{2+} videos were acquired at 20 frames/sec using a Miniscope Data Acquisition PCB and Data Acquisition Software ([50], Table S1). We acquired images with a field of view of 720×480 pixels (approximately 800 µm × 600 µm). Excitation LED power was adjusted to optimize imaging for each animal with a maximum output of 1 mW. To avoid bleaching GCaMP6f, no trials were longer than 10 min.

Elevated zero maze (EZM) and variations. To assay anxiety-like behavior, we used the EZM, an elevated circular arena with two open arms and two closed arms (track diameter = 50 cm, track width = 5 cm, wall height for closed arms = 14 cm, height of track = 63.5 cm). Open arms are considered anxiogenic and closed are anxiolytic. Mice were initially placed in the closed arm and recorded for 10 min [51].

Several variations on the normal EZM were used. Some animals performed this task twice, either one hour or one day apart. Other animals performed this task under different lighting settings. Dim light EZM was carried out at 20 lux, as opposed to the standard 200 lux. In addition, some animals were tested in the Platform EZM. This is a modified EZM in which a clear acrylic ring (track diameter = 50 cm, track width = 5 cm) is attached to the top of the normal EZM, so it sits about 14 cm higher than the normal track and has no closed arms. For this task, the lighting in the room was increased to 400 lux.

Open field (OF). To assay anxiety-like behavior and locomotion, the OF was used. The center of the arena is considered anxiogenic and the periphery is anxiolytic. Mice were placed in the center of a custom-made acrylic arena ($50 \times 50 \times 30$ cm length-width-height) and allowed to explore for 10 min.

Social tasks. For all social tasks, the arena contained two mesh wire cups – one on each end of the arena ($50 \times 25 \times 30.5$ cm length-width-height). In each trial, the experimental mouse was placed in the center of the arena and given 5–10 min to explore the arena and cups. The side of the arena with each stimulus was randomized between trials and animals.

In Sociability (Day 1), one mesh wire cup housed a littermate and the other was empty. In Social Novelty (Days 2 and 3), one cup housed a littermate and the other housed an entirely novel male CD-1. These tasks were each 10 min per day.

In multi-trial Social Interaction, there were 3 trials for 5 min each with a 10 min inter-trial interval (ITI). In all 3 trials, one cup contained a stimulus mouse and the other remained empty. The stimulus animal was a male CD-1 that was entirely novel in Trial 1 and was used across all 3 trials. The side of the arena where the stimulus mouse was placed was randomized between animals and trials.

Object interaction. In the multi-trial Object Interaction task, mice were allowed to freely explore a rectangular arena ($50 \times 25 \times 30.5$ cm length-width-height). To assay repeated interactions with an object, a novel object was placed at one end of the arena and the animal was given 5 min to explore. This was repeated over 3 trials with a 10 min ITI. The object was entirely novel at the start of Trial 1 and the same object was used for all 3 trials. The side of the arena where the object was placed was randomized between animals and trials. All objects were small, plastic toys of various shapes.

Behavioral assays for c-Fos experiments. Mice were either exposed to the platform EZM (described above) or were controls. The EZM animals were allowed to freely explore the Platform EZM for 15 min and were then removed from the arena and returned to their home cage. Control mice were briefly handled two times, 15 min apart. 2 h after either handling or Platform EZM, animals were perfused for tissue collection and IHC.

Behavioral analysis

During behavioral tasks, the movement of mice was tracked using DeepLabCut (DLC) [52], an open-source program that uses machine learning to track body parts in behavioral videos, as described by Comer et al. [53]. To assess accuracy, videos labeled by the software were inspected by a trained observer and custom MATLAB (MathWorks, Natick, Massachusetts) scripts were used to verify that DLC located each body part at least 95% of the total time the animal was tracked. For EZM and OF, we tracked the centroid of the mouse's body to determine velocity, distance traveled, and when the mouse was in each zone of the arena. For the OF, we divided the arena into 25 squares (10×10 cm each) and defined the periphery as the outermost 16 and the remaining 9 as the center. For the social and object tasks, we tracked the head to determine close proximity to either cup or to the object. Binary behavior matrices (vectorized behavior) indicating the location of the animal were created from DLC using custom MATLAB scripts.

Ca^{2+} imaging analysis

Ca^{2+} imaging data were processed using CaImAn [54] written in Python (https://www.python.org/). Ca^{2+} recordings underwent piecewise rigid motion correction using patches of 48×48 pixels with 24×24 pixel overlap. Following image stabilization, cell detection and extraction of deltaf/f (df/f) traces were performed with a merging threshold of activity correlation greater than 0.7 between nearby cells and a 2.5 minimum threshold for the signal to noise ratio. df/f traces and spatial information were exported and saved in.mat format using SciPy [55]. All subsequent analysis was performed using custom MATLAB and Python functions. Raw Ca^{2+} traces were z-scored using the mean baseline df/f and sigma from the entire time series for each trial. Z-scored traces report df/f values in units of standard deviation (SD). A binary filter was applied to all cells based on peaks of Ca^{2+} transients [56] and select cells were excluded for noise based on a threshold of 0.4 peaks/sec. Due to the different acquisition frequencies of behavioral and Ca^{2+} imaging videos, data were aligned using timestamps from acquisition and custom MATLAB scripts. Gaps in neural data due to dropped frames (less than 1% of the total frames) were filled with averaged z-scored df/f values from surrounding frames. Starts and ends of behavioral epochs were matched to Ca^{2+} data timestamps to isolate neural activity during select behaviors.

Ca^{2+} activity. For all figures, Ca^{2+} activity refers to the area under the curve. To quantify this value, we used z-scored df/f traces and took their integral using the MATLAB trapz function. For all figures, excluding Fig. S1Q and S, area under the curve was calculated for 5 sec intervals, which was chosen based on average transient length. When calculating the average area under the curve across velocities (Fig. S1Q and S), the intervals were 1 sec. These integral values were calculated for each cell to get the Ca^{2+} activity values. When average Ca^{2+} activity is reported, that refers to the average area under the curve for all cells for each mouse.

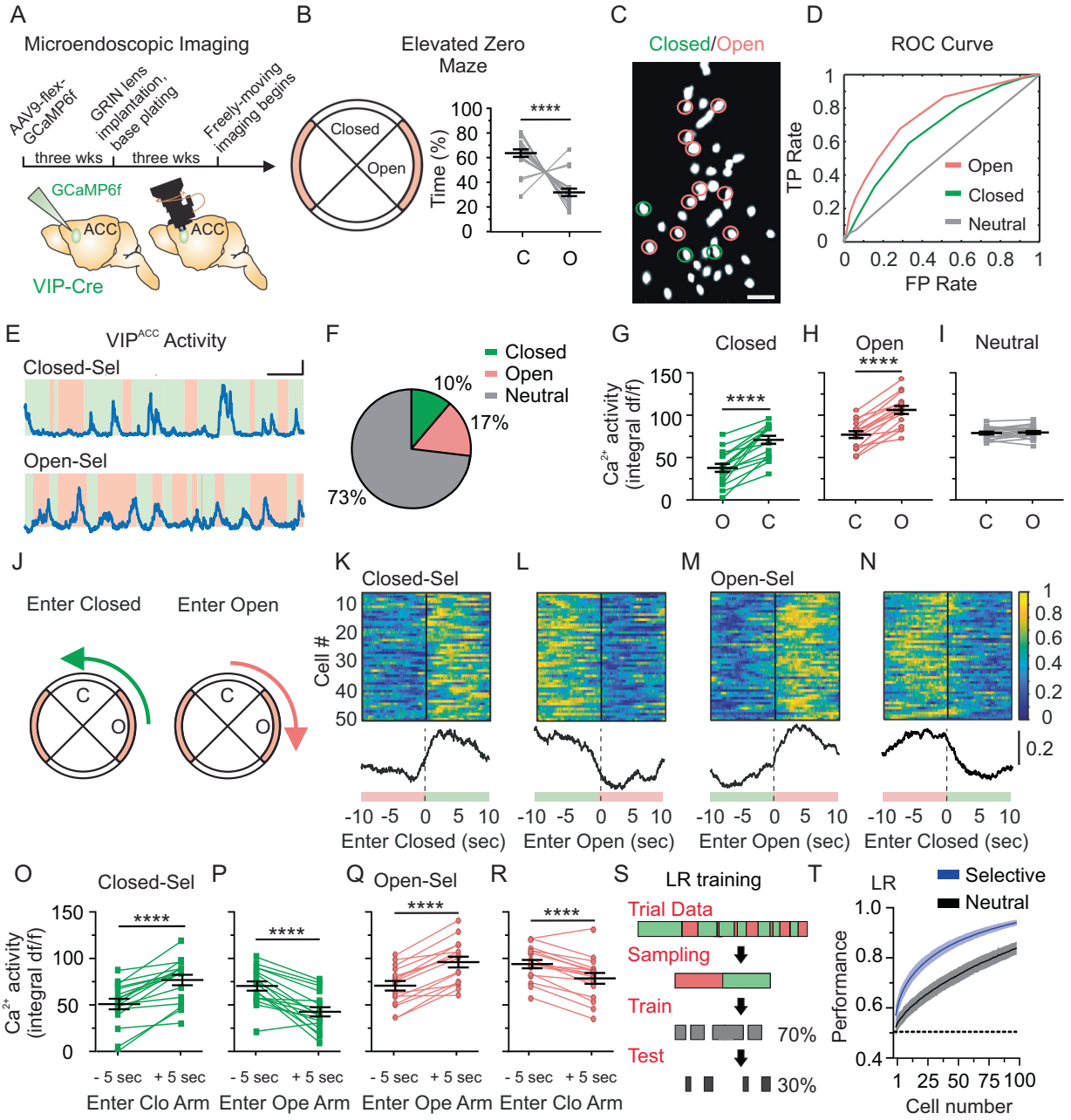

Single cell ROC analysis. Responses of individual cells during different behavioral conditions were assessed within each behavioral trial using receiver operating characteristic (ROC) analysis, as previously described [57]. The ROC curve demonstrates how well a single neuron's activity matches an animal's behavioral state, which can be quantified by calculating the area under the ROC curve (auROC) [57, 58]. For each neuron in each behavioral condition, a ROC curve was generated using the true positive rate (TPR) and false positive rate (FPR) values for that cell and behavioral state. TPR and FPR were calculated across multiple binary thresholds applied to z-scored df/f traces of each cell, ranging from the minimum to maximum values of the Ca^{2+} signal. For each threshold, binarized df/f traces were compared to the binary behavioral vectors, which used binary values to indicate an animal's presence or absence in a specific zone of the arena. TPR and FPR were then plotted against each other to create each ROC curve and auROC was calculated.

To classify cells as stimulus-selective or neutral, we determined whether the cell's auROC value for a given stimulus was high enough to suggest it preferentially activated to a stimulus. To do this while accounting for any random alignment in our data, we calculated 1000 null values for each cell by applying circular permutations of randomized lengths to the Ca^{2+} data and calculating auROC for each of these randomized versions of the data. Cells were considered selective for a certain stimulus if the auROC of that cell was at least 2 SD greater than the mean of the null distribution. If a cell was not selective for any of the stimuli in a given task, it was classified as a "neutral cell".

auROC analysis across tasks or trials. To determine if the same cells were responsive to different stimuli or if they were stable across trials, we registered cells across EZM and OF or multiple trials of EZM, social, and object tasks using CaImAn [54]. For each cell and behavioral condition, auROC was calculated. To assess stability, cell selectivity was determined for a given trial and those same cells were monitored in another trial or task. To control for the possibility of cell-selectivity classifications overlapping by chance, we randomly assigned cell IDs to different selective cells. Using the real percentage of selective cells in our dataset but different cell IDs, we shuffled the data (1000 iterations, circular shift) and compared it to the real data. For Figs. 4H and 5H the real and control overlap data were plotted across trials.

Fig. 1 VIP^{ACC} encode diverse contexts in the EZM. A Experimental timeline. **B** Left: EZM. Pink zone: open arms. White zone: closed arms. Right: Time spent in each EZM arm type (%). Closed vs. Open. $N = 19$. ****$p < 0.0001$. Trial duration = 10 min. **C** Representative image of VIP^{ACC} expressing GCaMP6f (white) in vivo while the mouse navigates the EZM. Pink circles: open-selective, green circles: closed-selective. Neutral cells are not circled. Scale bar = 50 μm. **D** ROC curves for 3 representative neurons demonstrating how well cells encode behavioral states. An open-selective (pink, auROC = 0.75), a closed-selective (green, auROC = 0.71), and a neutral (gray, auROC = 0.51) VIP^{ACC}. **E** Representative Ca^{2+} transients from selective cells: closed-selective (top), open-selective (bottom). Shaded areas indicate the location of the mouse: open (pink) or closed (green) arms. Scale bar = 25 s and 2 SD. **F** 17% of VIP^{ACC} were classified as open-selective, 10% as closed-selective, and 73% as neutral. **G–I** Average Ca^{2+} activity of selective VIP^{ACC} in the EZM. $N = 19$ mice, $n = 1171$ cells. **G** Closed-selective. Closed vs. Open. ****$p < 0.0001$. $N =$ 17 mice, $n = 110$ cells. **H** Open-selective. Open vs. Closed. ****$p < 0.0001$. $N = 16$ mice, $n = 203$ cells. **I** Neutral cells. Closed vs. Open. $p = 0.7100$. $N = 19$ mice, $n = 858$ cells. **J** Movement of a mouse from an open to a closed arm (left) or a closed to an open arm (right) of the EZM. **K–N** Heatmaps (top) show activity of individual selective cells during behavioral transitions. The activity of each cell is normalized and presented on a scale from 0 (dark blue, least active) to 1 (yellow, most active). Traces (bottom) show normalized average activity of selective cells during these transitions. Shaded areas (bottom) indicate the location of the mouse: open (pink) or closed (green) arms. **K, L** Activity of closed-selective cells from 10 s prior to 10 s after entering either a closed (**K**) or an open (**L**) arm. Activity of open-selective cells from 10 s prior to 10 s after entering either an open (**M**) or closed (**N**) arm. **O–R** Average Ca^{2+} activity of selective-cell. **O** Closed-selective entering closed arm. −5 vs. +5 s. ****$p < 0.0001$. $N = 17$ mice. **P** Closed-selective entering open arm. −5 vs. +5 s. ****$p < 0.0001$. $N = 17$ mice. **Q** Open-selective entering open arm. −5 vs. +5 s. ****$p < 0.0001$. $N = 16$ mice. **R** Open-selective entering closed arm. −5 vs. +5 s. ****$p < 0.0001$. $N = 16$ mice. **S** Schematic for logistic regression (LR) analysis. Red and green shading represent data from open and closed arms in the EZM, which were both used for training and testing. In total, 70% of frames were used to train the LR and 30% to test. **T** LR performance when trained with either Ca^{2+} data from selective cells (blue) or neutral cells (black) in the EZM. Shaded regions in the curves are the SD: Selective cells: light blue. Neutral cells: gray. All statistics performed with Paired *t* test. For panels G-I and O-R, Ca^{2+} activity refers to the area under the curve (integral df/f). Each ROC curve and trace is from one representative neuron. Each replicate in (**B**), (**G–I**), and (**O–R**) represents one mouse. ROC receiver operating characteristic, TP true positive rate, FP false positive rate, C closed arm, Clo closed arm, O open arm, Ope open arm, Closed-sel closed selective, Open-sel open-selective, df/f Deltaf/f, LR logistic regression.

auROC analysis validation. To validate the auROC analysis (Fig. S1W), we looked for consistent activity changes in the cells we identified as selective. We calculated auROC values using the first half of the EZM or Sociability data, rather than the entire dataset, to identify selective cells (Fig. S1W). Next, using these selectivity classifications, we assessed Ca^{2+} activity from the second half of the data under the cell's preferred and non-preferred conditions (Fig. S1W). The preferred condition was the context or stimulus that the cell was selective for, whereas non-preferred was the other condition in that task. To assess whether ROC analysis led to random assignment of cells as selective, we reran our analysis with Ca^{2+} traces that were temporally shifted at random lengths 1000 times. This allowed us to calculate the average percentage of cells assigned as selective in this randomized control.

EZM transition heatmaps and traces. For Fig. 1, we plotted heatmaps of the average activity of selective cells 10 sec before and after transitioning between arms in the EZM. The average traces from individual cells were normalized to their maximum value. The average trace of all selective cells during transitions was plotted below the heatmap.

Spatial heatmaps. For Fig. S2, the activity heatmaps were plotted to visualize the average cell activity in 5 × 5 pixel spatial bins across the OF arena. Z-scored df/f traces from individual cells were normalized to their maximum value and matched with DLC centroid coordinates at the closest timestamp.

Logistic regression. To determine whether VIP^{ACC} activity could be used to predict an animal's behavioral state, we used logistic regression (LR) analysis. First, data for a given behavior were combined by selecting frames when the animal was performing that behavior and the corresponding Ca^{2+} imaging data. 70% of these data were randomly assigned for training and the remaining 30% were used for testing the LR using the MATLAB function mnrval() and custom MATLAB code (Fig. 1S). The LR was trained and tested using an increasing interval of randomly selected cells with 1000 repetitions for each number of cells. For LR analyses over multiple behavioral trials, the LR was trained with 70% of the data from the first trial and tested with 30% of the data from the second trial using the same population of cells. LR performance was evaluated by using the MATLAB function mnrfit() and calculating the percent of correctly LR-predicted behavior states in the testing data. While our analyses assume that Ca^{2+} activity is uncorrelated in time, the biophysics of Ca^{2+} entry into the cell bodies as well as the kinetics of the fluorophore could introduce significant correlations which may bias the predictive power of selective vs neutral neurons if they have systematically differing correlation timescales. To ensure differing amounts of correlation over time did not bias LR performance [59], we calculated the autocorrelation function of the Ca^{2+} trace of individual neurons and fitted them to an exponential function to extract a timescale for the correlation. This autocorrelation time constants was not significantly different between the selective and neutral populations (data not shown).

Ex vivo electrophysiology

At least 3 weeks after viral injections, acute ACC brain slices were prepared as previously described in Melzer et al. [22]. Briefly, for whole-cell patch-clamp recordings, mice were deeply anesthetized with inhaled isoflurane and transcardially perfused with approximately 30 ml ice-cold sucrose solution oxygenated with carbogen gas (95% O_2, 5% CO_2, pH 7.4). Mice were quickly decapitated and brains were removed. 300 μm thick sections were cut on a VT 1000 S vibratome (Leica Biosystems, Buffalo Grove, Illinois) in an ice-cold oxygenated sucrose solution (252 mM sucrose, 3 mM KCl, 1.25 mM $Na_2H_2PO_4$, 24 mM $NaHCO_3$, 2 mM $MgSO_4$, 2 mM $CaCl_2$, and 10 mM glucose). Coronal slices were used for all experiments. Slices were incubated in oxygenated Ringer's extracellular solution (125 mM NaCl, 25 mM $NaHCO_3$, 1.25 mM NaH_2PO_4, 2.5 mM KCl, 2 mM $CaCl_2$, 1 mM $MgCl_2$, and 25 mM glucose) at 32 °C for ~15 min and were subsequently kept at RT until used for recordings. Whole-cell patch-clamp recordings were performed at 30–32 °C using pipettes pulled from borosilicate glass capillaries with resistances of 3-4 MΩ. Sections were continuously perfused with oxygenated extracellular solution. Cells were visualized using an upright microscope equipped with Dodt gradient contrast and standard epifluorescence (Olympus BX51, Olympus Corporation, Tokyo).

All electrophysiological recordings were acquired using Multiclamp 700B amplifier (Molecular Devices, San Jose, California), MultiClamp Commander (Molecular Devices, San Jose, California), and MTTeleClient for telegraphs. MATLAB was used to control current/voltage output and to visualize and store acquired data. Signals were sampled at 10 kHz. Liquid junction potentials were not corrected. Patch-clamp recordings were guided by a 60x/0.9NA LUMPlanFl/IR objective (Olympus, Tokyo). Pipettes and microscope movements were controlled with a motorized micromanipulator (MP-285, Sutter Instrument Co., Novato, California). The setup was equipped with a U-RFL-T fluorescence lamp (Olympus Corporation, Shinjuku, Tokyo, Japan), which allowed for the identification of VIP^{ACC} based on their EGFP expression.

Excitatory postsynaptic currents (EPSCs) were recorded in identified VIP^{ACC} cells that were voltage clamped at −70 mV. EPSCs were recorded with K^+-based low Cl^- intracellular solution (130 mM K^+-Gluconate, 10 mM Hepes, 10 mM Phosphocreatine-Na, 10 mM Na-Gluconate, 4 mM ATP-Mg, 4 mM NaCl, and 0.3 mM GTP, pH 7.2 adjusted with KOH). Series resistance was continuously monitored in voltage-clamp mode in response to small hyperpolarizing pulses. Series resistances of 35 MΩ were accepted for analyzing EPSCs in VIP cells.

Optogenetic experiments. During a whole-cell patch-clamp recording, RSC axonal projections were stimulated in acute brain slices with 473 nm light

(DPSS Laser System, Laserglow Technologies, Toronto, Canada) at 20 mW through a 40x objective. To block polysynaptic inputs and reveal direct synaptic RSC-ACC connections, TTX (1 µM) and 4-AP (100 µM) were added to the bath 5 min prior to EPSC recordings. Two 5 msec long light pulses with a 50 msec interval were used every 20 sec. Traces were averaged over at least 9 stimulations to reveal responding cells and to distinguish small responses from noise.

Perfusions and histology

Animals were perfused to visualize viral injections and lens placements. Mice were injected with an overdose of sodium pentobarbital (250 mg/kg; IP, Vortech Pharmaceuticals Ltd., Dearborn, Michigan) and transcardially perfused with phosphate buffered saline (PBS) followed by 4% paraformaldehyde (PFA) in PBS. Brains were extracted, stored in PFA for 24 h at 4 °C, and then transferred to a 30% (w/v) sucrose solution for 48 h at 4 °C. Tissue was sectioned at 40–100 µm using a freezing sliding microtome (SM2000, Leica Biosystems, Buffalo Grove, Illinois). Sections were mounted onto slides (Globe Scientific Inc., Mahwah, New Jersey) using Fluoromount-G mounting medium with DAPI (Thermo Fisher Scientific, Waltham, Massachusetts) to visualize nuclei.

Immunohistochemistry

To visualize calretinin (CR) or cholecystokinin (CCK) in c-Fos experiments or to improve visibility of EGFP in rabies tracing experiments, sectioned brain tissue was stained using IHC. First, tissue was washed in PBS for 10 min 3 times. Next, sections were blocked and permeabilized in PBS with 10% normal goat (for c-Fos experiments) or donkey (for rabies experiments) serum and 0.25% TritonX100. Sections were then transferred to a solution of PBS, 10% goat or donkey serum, and the primary antibodies and were incubated at 4 °C. For c-Fos experiments, each section was stained for c-Fos and either CR or CCK and incubated for 48 h. For rabies experiments, any tissue at or near the injection site that could have EGFP expression was stained for EGFP and incubated for 24 h. Primary antibodies used were mouse anti-c-Fos (1:250, #ab208942, Abcam, Cambridge), rabbit anti-CCK (1:200, #C2581, Sigma Aldrich, St. Louis, Missouri), guinea pig anti-CR (1:500, #CRgp7, Swant, Burgdorf), and chicken anti-GFP (1:1000, #ab13970, Abcam, Cambridge). After incubation, tissue was rinsed in PBS with 0.025% TritonX100 for 10 min 3 times and then incubated with secondary antibodies in PBS for 4 h (c-Fos experiments) or 2 h (rabies experiments). Secondary antibodies used were goat anti-mouse 555 (1:500, #A21422, Thermo Fisher Scientific, Waltham, Massachusetts), donkey anti-rabbit 647 (1:250, #A-31573, Thermo Fisher Scientific, Waltham, Massachusetts), llama anti-guinea pig 647 (1:500, #80308, Progen, Heidelberg), and donkey anti-chicken 488 (1:1000, #703-545-155, Jackson ImmunoResearch Laboratories Inc., West Grove, Pennsylvania).

Imaging and histological analysis

Sections were imaged using an upright wide-field or inverted laser scanning confocal microscope (Nikon Eclipse Ni or Nikon Eclipse Ti with C2Si+ confocal, Nikon Instruments Inc., Melville, New York) controlled by NisElements (4.20, Nikon Instruments Inc., Melville, New York). Images were acquired using a Plan Fluor 4X (NA 0.13), 10X (NA 0.3), or a Plan Apo λs 40X (NA 1.3) objective with standard Nikon HQ filter cubes for DAPI, EGFP/GCaMP/Alexa Fluor-488, mCherry/Alexa Fluor-555, and Alexa Fluor-647.

Images were analyzed as TIFFs in ImageJ (National Institute of Health, Bethesda, Maryland) and compared to a brain atlas [60, 61] (brain-map.org/api/index.html) to identify brain regions. Cell distance from pia was calculated by first identifying the lens location in the brain section using a brain atlas [60, 61] and then by calculating the lateral distance of each cell from the edge of the field of view of an in vivo Ca^{2+} recording. To quantify layer specificity of starter cells in the rabies tracing data, brain sections were compared to a brain atlas [60, 61]. For each cell type, the layer of each starter cell was identified manually by trained observers and quantified [60, 61].

To quantify c-Fos activity and molecular markers in VIP^{ACC}, GFP positive cells were identified and ROIs were drawn around each cell of interest by trained observers using ImageJ. These ROIs were then inspected for the presence or absence of CR or CCK. The intensity value in the c-Fos channel for each ROI and the average background signal for each brain slice was quantified in ImageJ. To binarize cells as either c-Fos positive or negative, we calculated an intensity threshold (average background intensity × 1.5) and classified cells as c-Fos positive if their intensity value was higher than this threshold. This strategy controlled for differences in staining quality and led to classification of approximately 50% of cells (top two quartiles) as c-Fos positive. These data were used to calculate the percentage of c-Fos positive or negative VIP cells that were positive for different markers in control and EZM-exposed mice. All c-Fos values for each molecular subtype were normalized to the mean % of c-Fos positive cells in control animals for that marker and these normalized values were plotted for control and EZM-exposed animals.

Analysis of rabies tracing data

For retrograde mapping experiments, brains were scanned to identify signal from starter and retrogradely-labeled input neurons. Cells were quantified using ImageJ. Starter cells were defined as cells that were positive for both GFP (from AAV-TVA-Glyco) and mCherry (from EnvA-ΔG-mCherry). We confirmed with DAPI that starter and retrogradely-labeled cells had a nucleus. Because each animal had a different number of starter cells, we normalized our data by dividing the number of retrogradely-labeled neurons in each region by the number of starter cells for that mouse (inputs per starter cell). The number and location of labeled neurons in a given region was independently confirmed by 3 trained scientists. After quantifying all cells, input brain regions were divided into quartiles by number of input neurons. Only brain regions in the top two quartiles were graphed and included in the percentage of cells per area, as presented in the Results section. We did not include EnvA-ΔG-mCherry inputs at the site of the ACC injection since leakage in TVA expression could lead to Cre-independent local labeling [62].

Statistical analysis

Statistical analyses were performed using Graph Pad Prism 8.0 (GraphPad Software Inc., San Diego, California) and MatLab. For figure preparation, CorelDRAW Graphics Suite X8 (Corel Corporation, Ottawa, Canada) and ImageJ were used. The threshold for significance was set to $\alpha = 0.05$ and $^{*}p < 0.05$, $^{**}p < 0.01$, $^{***}p < 0.001$, $^{****}p < 0.0001$. Data are presented as mean ± SEM, unless otherwise noted. *T* tests and ANOVAs followed by appropriate post tests were used and are specified in the figure legends. Frequency distributions were fitted with Gaussians and percentages of selective cells are represented in pie charts. Numbers of animals and cells for each experiment are listed in each figure legend.

RESULTS

VIP interneurons in the ACC encode diverse contexts in the EZM

To determine whether individual VIP cells in the ACC (VIP^{ACC}) show stimulus preference, we imaged their Ca^{2+} activity as mice explored the elevated zero maze (EZM), an assay of anxiety-like behavior in rodents. To do this, we injected AAV9-flex-GCaMP6f and implanted GRIN lenses into the ACC of VIP-Cre mice (Fig. 1A, Fig. S1A–H). 3D-printed miniscopes that detach from baseplates were adapted from two previous designs [42, 49], assembled in-house, and used for Ca^{2+} imaging. Post-mortem histology showed that injections and lenses were successfully targeted to the ACC (Fig. S1G), allowing for monitoring of VIP^{ACC} with single-cell resolution in awake, behaving animals (Fig. S1I, J). This histology also showed damage to secondary motor cortex (M2) from lens implantation (Fig. S1G). However, comparing behavior of these animals to non-implanted controls in the open field (OF) showed that this damage did not cause locomotor impairments (Fig. S1N, O).

The EZM was used to quantify anxiety-like behavior – closed arms are anxiolytic and open arms are anxiogenic (Fig. 1B). To determine whether lens implants and miniscopes interfered with normal anxiety-related behavior, we compared the behavior of miniscope-mounted animals to controls. No differences were found, suggesting that neither surgeries nor implants altered these behaviors (Fig. S1M (OF) and T (EZM)). In support of this, implanted mice spent less time in the open arms of the EZM than in the closed (50% decrease, Fig. 1B).

We monitored Ca^{2+} dynamics while animals navigated the EZM to determine whether VIP^{ACC} activity changed during exploration of anxiogenic contexts. When looking at the whole VIP^{ACC} population, average Ca^{2+} activity increased when animals were

in the open arms, as compared to the closed arms (5% increase, Fig. S1R), suggesting that VIP^{ACC} preferentially activate to anxiogenic contexts. However, it was unclear whether VIP^{ACC} were homogeneous in their stimulus preference (all uniformly activating to anxiogenic contexts) or functionally heterogeneous (individual neurons preferentially activating to different contexts). To test this, we extracted Ca^{2+} traces and performed receiver operating characteristic (ROC) analysis on each VIP^{ACC} [57] (Fig. 1C–E). This analysis provided us with area under the curve ROC (auROC) values (Fig. 1D, Fig. S1U, V), which quantify how well a cell's activity matches a behavioral state; higher auROCs reflect better encoding of the behavioral state. For each VIP^{ACC}, auROC was calculated for each EZM arm type. Using this approach, we determined whether individual VIP^{ACC} demonstrated selectively increased activity in one context and classified them as open-selective (17% of analyzed cells), closed-selective (10%), or neutral (not selective for either stimulus, 73%) (Fig. 1C–F). When these data were shuffled 1000 times as a control (circular shift), 5% of cells were selective for each stimulus (data not shown), suggesting that the percentage of selective cells identified did not occur entirely by chance. Closed-selective cells showed increased activity while animals were in the closed, as compared to the open arms (46% increase, Fig. 1E, top and G), whereas open-selective cells showed the opposite effect (37% decrease, Fig. 1E, bottom and H).

To determine whether selective VIP^{ACC} activity rapidly changes when mice enter the closed or open arm, we isolated epochs (20 sec windows) when animals transitioned from one arm to another (Fig. 1J) and plotted VIP^{ACC} activity. Heatmaps, traces, and average Ca^{2+} activity of selective cells showed robust differences during behavioral transitions (Fig. 1K–R). Closed-selective cells preferentially activated soon after animals entered the closed arms (33% increase, Fig. 1K and O) or prior to entering the open arms (38% increase, Fig. 1L and P). Open-selective cells preferentially activated soon after animals transitioned into the open arms (16% increase, Fig. 1M and Q) or before leaving the closed arms (26% increase, Fig. 1N and R). Notably, most VIP^{ACC} were neutral and did not preferentially activate to either context (Fig. 1I, and see Fig. S1U, V, for distribution of auROC values).

To determine whether VIP^{ACC} activity could be used to encode animal behavior, we used logistic regression (LR) (Fig. 1S, T). When the LR was trained with neural data from selective cells, as compared to neutral cells, it better predicted behavior (Fig. 1T, selective vs. neutral, 20% or 13% increase in performance, for $n =$ 50 or 100 cells, respectively; and no overlap between SD bands (shaded regions) of selective and neutral cells). LR performance also improved as more cells were used in training, suggesting that these cells may encode information as groups of inhibitory neurons. We next used half of our data (first 5 min of the recordings) to identify selective cells and used those classifications to quantify average Ca^{2+} activity in the remaining half (Fig. S1W). In this second half, average activity of selective cells increased when mice were in the preferred context, relative to the non-preferred (23%, EZM, Fig. S1W). This verified that our auROC analysis was reliable and suggested that stimulus-selectivity was consistent within a trial.

We next assessed whether these findings were context-specific, or if they would be recapitulated in another task that assayed anxiety-like behavior. Similar to their behavior in the EZM, mice in the OF avoided the anxiogenic center zone (79% more time in periphery, Fig. S1K, L). We found zone-specific cells that encoded the animal's behavioral state (Fig. S2), although there was no significant difference in overall VIP^{ACC} activity as animals explored the two zones (Fig. S1P).

To determine whether locomotion impacted VIP^{ACC} activity, we monitored animal velocity. In the OF, there was no relationship between velocity and VIP^{ACC} activity (Fig. S1Q). However, in the EZM, there was a difference in overall VIP^{ACC} activity at different velocities (Q1 vs. Q4: 11% increase, Fig. S1S), suggesting that VIP cell activity in the ACC was modulated by velocity. However, further data analysis demonstrated that closed-selective cells did not exhibit velocity modulation (effect of velocity quartile on Ca^{2+} activity. Repeated measures ANOVA. Closed-selective: $F_{(2.029,32.47)} = 1.557$, $p = 0.2260$. Open-selective: $F_{(2.613,41.80)} = 15.06$, $^{****}p < 0.0001$). Therefore, modulation of Ca^{2+} activity by velocity is insufficient to fully explain the selective encoding of different EZM contexts. In support of this, although the Ca^{2+} activity of neutral cells was modulated by velocity (effect of velocity quartile on Ca^{2+} activity. Repeated measures ANOVA. Neutral: $F_{(1.787,32.17)} = 6.518$. $^{**}p = 0.0054$), it was unchanged as animals explored different contexts (Fig. 1I).

VIP^{ACC} are heterogeneous in their molecular identity. Therefore, we investigated whether these differences could correlate with the functional heterogeneity found in vivo. We assayed whether VIP^{ACC} that express particular molecular markers activated differently when mice explored anxiogenic environments relative to control mice, by virally tagging VIP^{ACC} with EGFP (Fig. S3A) and using IHC to quantify levels of c-Fos (a proxy for neural activity, Fig. S3). Animals were either exposed to an anxiogenic environment (a version of the EZM with a higher platform, no closed arms, and brighter lighting) or briefly handled as a control. There was no significant difference in overall c-Fos levels of VIP^{ACC} in EZM-exposed mice versus controls (Fig. S3B). In addition, there was no significant difference in EZM-induced c-Fos between VIP cells that were positive or negative for 2 different molecular markers (Fig. S3C–G). We also assessed whether functional heterogeneity among the cells from our Ca^{2+} imaging correlated with differences in cortical depth, and found no difference in the localization between closed-selective, open-selective, or neutral cells (Fig. S3H–J). These results suggest that neither molecular identity nor cortical depth explains differences in activation to the EZM. Thus, open- and closed-selective cells likely comprise two populations of VIP^{ACC} with mixed molecular identities.

Subpopulations of VIP^{ACC} preferentially activate to social or non-social stimuli

Since VIP^{ACC} were functionally heterogeneous in anxiogenic environments, we investigated whether this diversity could be observed in other behavioral contexts. We first determined whether VIP^{ACC} were selective for social or non-social stimuli by recording their activity during Sociability and Social Novelty (Fig. 2A). In Sociability, mice explored a chamber with an empty mesh wire cup (which they had been acclimated to) and a littermate in a mesh wire cup (Fig. 2A). In Social Novelty, the cups housed either a littermate or a novel mouse (Fig. 2A). Implanted mice spent more time with their littermate than the empty cup (1.8 fold-change, Fig. 2B) and more time with the novel mouse than their littermate (1.5 fold-change, Fig. 2C), suggesting that they were interested in investigating other mice and had a preference for novel social stimuli.

Using ROC analysis, we identified stimulus-selective cells and demonstrated that they better encoded behavior than neutral cells (Fig. 2D–G). In Sociability, cells were classified as cup-selective (14%), littermate-selective (10%), or neutral (75%) (Fig. 2G). In Social Novelty, cells were classified as littermate-selective (10% Day 2, 17% Day 3), novel mouse-selective (19%, 13%), or neutral (71%, 69%, Fig. 2G). Interestingly, very few cells were selective for both stimuli in a trial (1% littermate- and cup-selective, <1% littermate- and novel mouse-selective, Fig. 2G). When data were shuffled 1000 times as a control (circular shift), 5% of cells were selective for each stimulus (data not shown), suggesting that the observed percentages of selective cells did not occur entirely by chance (Fig. 2G). Littermate-selective cells showed increased activity when animals interacted with the littermate, as compared to the cup (43% increase, Fig. 2F, top and H) or novel mouse (17% increase, Fig. 2J). Cup-selective VIP^{ACC}

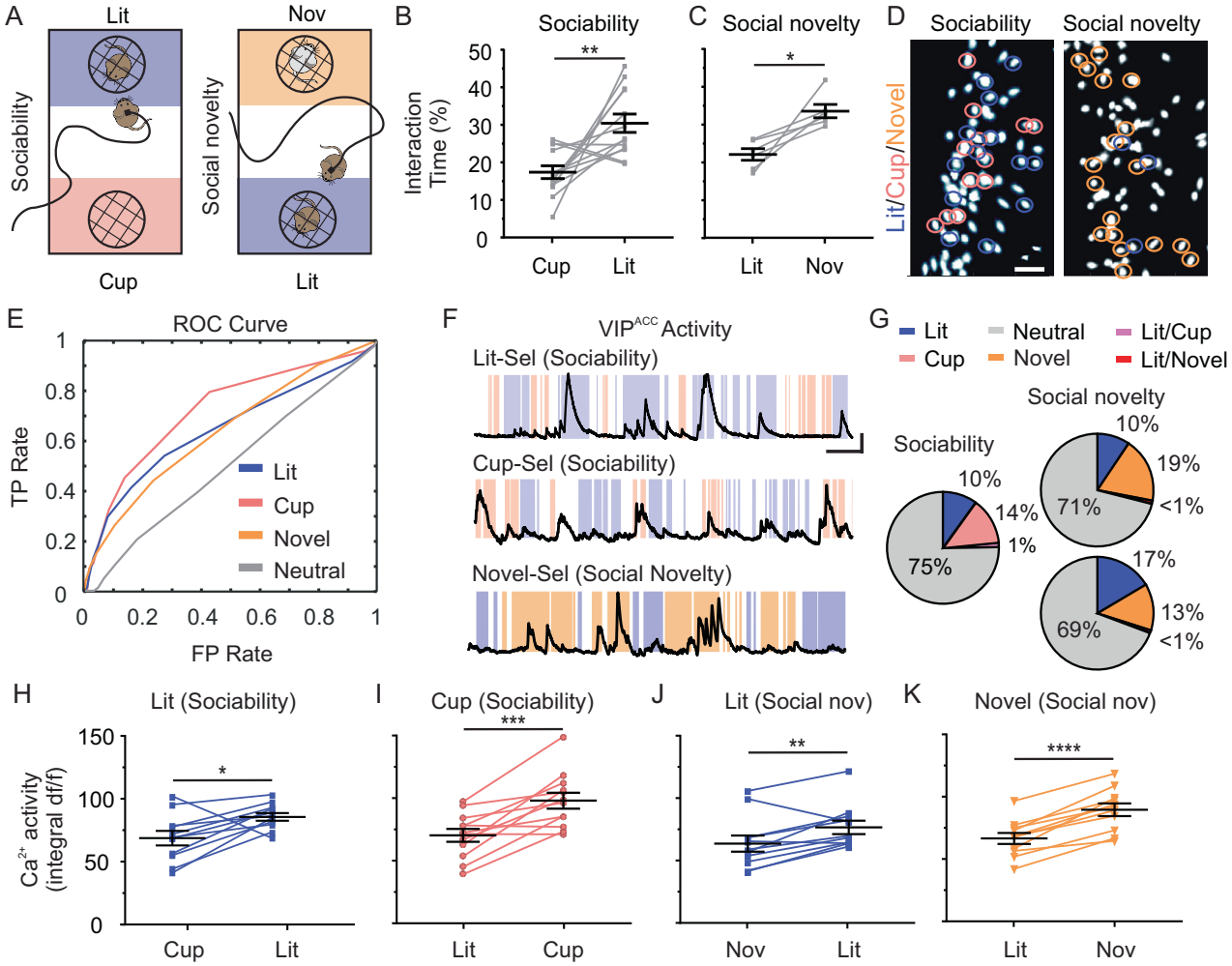

Fig. 2 VIP^{ACC} encode diverse stimuli in a social task. A Behavioral paradigm. Left: Sociability (Day 1). Right: Social Novelty (Days 2 and 3). Littermate zone (purple). Empty cup zone (pink). Novel mouse zone (orange). Neutral zone (white). **B** Sociability. Interaction Time (%). Cup vs. Littermate. $^{**}p = 0.0051$. $N = 13$. Trial duration = 10 min. **C** Social Novelty. Interaction Time (%). Littermate vs. Novel mouse. $^{*}p = 0.0121$. $N = 6$. Trial duration = 10 min. **D** Images of VIP^{ACC} expressing GCaMP6f (white) in vivo during Sociability (left) or Social Novelty (right). Pink circles: cup-selective, purple circles: littermate-selective, orange circles: novel mouse-selective. Neutral cells are not circled. Scale bar = 50 µm. **E** ROC curves for representative VIP cells: littermate-selective (purple, auROC = 0.65), novel-mouse-selective (orange, auROC = 0.64), cup-selective (pink, auROC = 0.73), and neutral (gray, auROC = 0.51). **F** Ca^{2+} transients of representative cells: littermate-selective (top), cup-selective (middle), novel mouse-selective (bottom). Shaded areas indicate location of mouse: littermate (purple), cup (pink), novel (orange), and neutral (white) zones. Scale bars = 25 s and 1 SD. **G** In Sociability, 14% of VIP^{ACC} were classified as cup-selective, 10% as littermate-selective, 1% as selective for both cup and littermate, and 75% as neutral. In Social Novelty, VIP^{ACC} were classified as littermate-selective (10% Day 2, 17% Day 3), novel-mouse-selective (19% Day 2, 13% Day 3), selective for both littermate and novel (<1% Day 2 and 3), and neutral (71% Day 2, 69% Day 3). $N = 13$ mice. For Sociability, $n = 662$ cells, for Social Novelty, $n = 354$ cells on Day 2 and 203 cells on Day 3. **H–K** Average Ca^{2+} activity of selective cells per mouse. **H** Littermate-selective cell during Sociability. Littermate vs. cup. $^{*}p = 0.0179$. $N = 11$ mice. $n = 68$ cells. **I** Empty cup-selective during Sociability. Cup vs. littermate. $^{***}p = 0.0006$. $N = 12$ mice. $n = 59$ cells. **J** Littermate-selective during Social Novelty. Littermate vs. novel mouse. $^{**}p = 0.0085$. $N = 11$ mice. $n = 59$ cells. **K** Novel-mouse-selective during Social Novelty. Littermate vs. novel mouse. $^{****}p < 0.0001$. $N = 11$ mice. $n = 63$ cells. All ROC curves, traces, and images are representative. Each replicate in (**B**) and (**C**) and (**H–K**) represents one mouse. All statistics performed with Paired *t* test. Lit littermate, Nov novel mouse, Lit-sel littermate-selective cell, Cup-sel cup-selective cell, Social nov social novelty, df/f Deltaf/f, ROC receiver operating characteristic, TP true positive, FP false positive.

were more active when animals interacted with the cup than the littermate (29% increase, Fig. 2F, middle and I). Novel mouse-selective neurons demonstrated higher activity while mice interacted with novel mice, rather than littermates (26% increase, Fig. 2F, bottom and K). Similar to the OF and EZM data, most cells were classified as neutral and their activity did not change as mice interacted with various stimuli (Fig. 2G, Fig. S4A–D, distribution of auROC values, and Fig. S4E, F). Similar to the EZM analysis, we used half of our data (first 5 min of the recordings) to identify selective cells and used those classifications to quantify average Ca^{2+} activity on the remaining half (Fig. S1W). In this second half, activity of selective cells increased when mice were in the preferred context, relative to the non-preferred (17%, Fig. S1W). This verified that our auROC analysis was reliable and suggested that stimulus-selectivity was consistent within a trial. Average activity of all VIP^{ACC} did not change as mice interacted with each stimulus (Fig. S4G, H), suggesting that, despite past research showing increased ACC activity during socialization [8], overall VIP^{ACC} activity does not change during interactions with other mice. These data demonstrate that individual VIP^{ACC}, as integral circuit elements, can participate in encoding of objects, other mice, or social novelty.

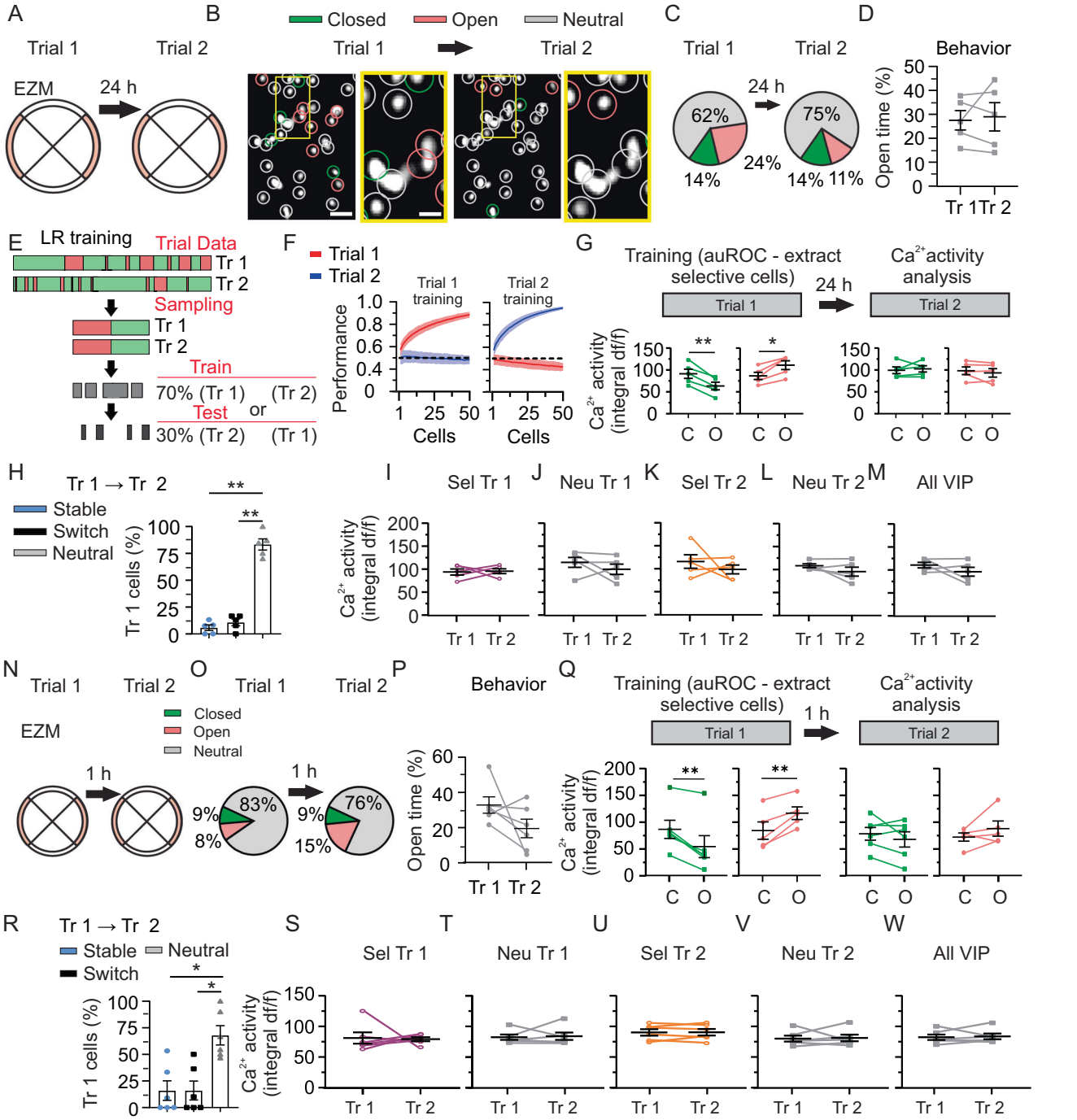

Stimulus-selective encoding of VIP^{ACC} is highly unstable in anxiety-related tasks across multiple timescales

To determine whether neuronal representations of anxiogenic stimuli in selective VIP^{ACC} subpopulations are stable across sessions, we monitored the same cells across multiple EZM trials. We first assessed VIP^{ACC} stability by placing animals in the EZM for 2 trials with an inter-trial interval (ITI) of 24 h (Fig. 3A). We were able to register data across trials to identify the same neurons and track their activity (Fig. 3B). We identified subpopulations of VIP^{ACC} that were open-, closed-selective, or neutral in each trial (Fig. 3B, C). The percentages of selective cells were not significantly different across trials (14% closed-selective, 24% or 11% open-selective, and 62% or 75% neutral) (Fig. 3C), which suggests population-level VIP^{ACC} encoding of these stimuli across several sessions (Trial x Selectivity: $F_{(2,12)} = 2.290$. $p = 0.1437$). When looking at individual neurons, however, we discovered that stimulus-selective activation was highly unstable over this 24 h period (Fig. 3B, E–H). The majority of cells identified as selective for a particular stimulus in one trial were no longer selective for that stimulus in the other (Fig. 3B, H).

We pursued this finding further by training a LR with neural data from one trial and assessing its performance in the other (Fig. 3E). When the LR was trained using cells identified as selective in Trial 1, its ability to predict behavior was much higher when tested on data from Trial 1, rather than Trial 2 (Fig. 3F, left, no overlap between SD bands (shaded regions) of Trial 1 and Trial 2 selective cells). The same pattern was found when Trial 2 data were used for training and Trial 1 was analyzed (Fig. 3F, right),

Fig. 3 Highly unstable VIP^{ACC} representations over multiple trials during an anxiogenic task. A–M Animals explored the EZM twice with a 24 h ITI. Data were registered to identify the same neurons in Trial 1 and 2 (24 h later). $N = 5$ mice, $n = 211$ cells. Trial duration = approximately 10 min. **A** Schematic showing behavioral pipeline for multi-trial 24 h ITI EZM. Pink: open arms, white: closed arms. **B** Images of VIP^{ACC} expressing GCaMP6f (white) in vivo during Trial 1 (left) and Trial 2 (right). The same cells were identified in both trials. Second and fourth images are zoomed versions of the yellow boxed regions. Pink circles: open-selective, green circles: closed-selective, gray circles: neutral cells. Scale bar = 50 µm in first and third images, 15 µm in second and fourth images. **C** In Trials 1 and 2, VIP^{ACC} were classified as closed-selective (green, 14% in Trial 1 and 2), open-selective (pink, 24%, 11%), or neutral (gray, 62%, 75%). Percentages of functional subtypes did not significantly change across trials. Two-way Repeated measures ANOVA. Selectivity: $F_{(2,12)} = 65.75$. ****$p < 0.0001$. Trial x Selectivity: $F_{(2,12)} = 2.290$. $p = 0.1437$. **D** % of time in open arm. Trial 1 vs. 2. $p = 0.7452$. **E** Schematic for logistic regression (LR) analysis. Red or green shading represents data from open or closed arms in the EZM, which were both used for training and testing. 70% of frames were used to train the LR and 30% to test. LR was trained and tested with either data from Trial 1 or 2. **F** LR trained with either Trial 1 (left) or Trial 2 (right) data and tested on Trial 2 (blue) or Trial 1 (red) data, respectively. Shaded regions are the SD. **G** Using selectivity classifications from Trial 1, Average Ca^{2+} activity was quantified for these registered cells in Trial 1 or 2. Top: Analysis schematic. Bottom: Ca^{2+} activity of Trial 1 selective cells in Trial 1 (left) and 2 (right). Green: closed-selective, pink: open-selective. Trial 1, closed-selective: Closed vs. Open. **$p = 0.0034$. Trial 1, open-selective: Closed vs. Open. *$p = 0.0112$. Trial 2, closed-selective: Closed vs. Open. $p = 0.6567$. Trial 2, open-selective: Closed vs. Open. $p = 0.3996$. **H** % of cells identified as selective in Trial 1 that were stable, switched selectivity, or were neutral in Trial 2. Repeated measures ANOVA. $F_{(1.145,4.582)} = 86.27$. ***$p = 0.0003$. Stable vs Switched. $p = 0.2360$. Stable vs Neutral. **$p = 0.0011$. Switched vs Neutral. **$p = 0.0020$. **I–M** Average Ca^{2+} activity for all selective or neutral cells as classified in Trial 1 (**I**, **J**) or 2 (**K**, **L**). **I** Trial 1 selective cells. Trial 1 vs. 2. $p = 0.8634$. **J** Trial 1 neutral cells. Trial 1 vs. 2. $p = 0.3816$. **K** Trial 2 selective cells. Trial 1 vs. 2. $p = 0.4642$. **L** Trial 2 neutral cells. Trial 1 vs. 2. $p = 0.2573$. **M** Average Ca^{2+} activity for all VIP^{ACC} in Trials 1 and 2. $p = 0.2751$. **N–W** Animals explored the EZM twice with a 1 h ITI. Data were registered to identify the same neurons in Trials 1 and 2. $N = 6$ mice, $n = 260$ cells. Trial duration = 7 min. **N** Schematic showing behavioral pipeline for 1 h ITI EZM. Pink: open arms, white: closed arms. The same cells were identified in both trials. **O** In Trials 1 and 2, VIP^{ACC} were classified as closed-selective (green, 9% in Trials 1 and 2), open-selective (pink, 8%, 15%), or neutral (gray, 83%, 76%). Percentages of functional subtypes did not significantly change across trials. Two-way Repeated measures ANOVA. Selectivity: $F_{(2,15)} = 273.0$. ****$p < 0.0001$. Trial x Selectivity: $F_{(2,15)} = 2.361$. $p = 0.1284$. **P** % of time in open arm. Trial 1 vs. 2. $p = 0.1681$. **Q** Using selectivity classifications from Trial 1, Average Ca^{2+} activity was quantified for these selective cells in Trial 1 or 2. Top: Analysis schematic. Bottom: Average Ca^{2+} activity of Trial 1 selective cells in Trial 1 (left) and 2 (right). Green: closed-selective, pink: open-selective. Trial 1, closed-selective: Closed vs. Open. **$p = 0.0022$. Trial 1, open-selective: Closed vs. Open. **$p = 0.0072$. Trial 2, closed-selective: Closed vs. Open. $p = 0.2980$. Trial 2, open-selective: Closed vs. Open. $p = 0.2326$. **R** % of cells identified as selective in Trial 1 that were stable, switched selectivity, or were neutral in Trial 2. Repeated measures ANOVA. $F_{(1.998,9.989)} = 7.345$. *$p = 0.0109$. Stable vs Switched. $p > 0.9999$. Stable vs Neutral. *$p = 0.0491$. Switched vs Neutral. *$p = 0.00448$. Average Ca^{2+} activity for all selective or neutral cells as classified in Trial 1 (**S**, **T**) or 2 (**U**, **V**). **S** Trial 1 selective cells. Trial 1 vs. 2. $p = 0.8809$. **T** Trial 1 neutral cells. Trial 1 vs. 2. $p = 0.8212$. **U** Trial 2 selective cells. Trial 1 vs. 2. $p = 0.9117$. **V** Trial 2 neutral cells. Trial 1 vs. 2. $p = 0.7664$. **W** Average Ca^{2+} activity for all VIP^{ACC} in Trials 1 and 2. $p = 0.7664$. Each replicate represents one mouse. All statistics performed with Paired *t* test unless otherwise noted. ITI inter-trial interval, Tr trial, LR logistic regression, C closed, O open, df/f Deltaf/f, auROC area under the receiver operating characteristic (ROC) curve, h hours, Sel selective, Neu neutral.

which suggests that neural activity from one trial cannot be used to accurately predict animal behavior in the other trial and supports the notion that individual VIP^{ACC} are unstable in their representations. Next, we used selective cells identified in Trial 1 to determine whether the Ca^{2+} activity of these cells was modulated across trials and behavioral states (Fig. 3G). Mirroring our one trial EZM data (Fig. 1), Ca^{2+} activity of Trial 1 closed-selective cells was higher when animals explored the closed arms (30% increase, Fig. 3G, left, green) and the opposite was observed for Trial 1 open-selective cells (28% decrease, Fig. 3G, left, pink). When these same Trial 1 selective cells were monitored in Trial 2, there was no significant difference in the activity of either closed- or open-selective cells as animals explored different arm types (Fig. 3G, right), suggesting that the selective cells in Trial 1 were no longer modulated by the preferred context in Trial 2. To determine how the identity of Trial 1 selective cells changed in Trial 2, we quantified the percent of Trial 1 selective cells that either remained selective for the same stimulus in Trial 2 (e.g., closed- to closed-selective, Stable), switched selectivity (e.g., closed- to open-selective, Switched), or were neutral in Trial 2 (e.g., closed-selective to neutral, Neutral) (Fig. 3H). Most selective VIP^{ACC} from Trial 1 were neutral in Trial 2 (83% of cells changed from selective to neutral, Fig. 3H). Additionally, approximately 11% of all cells switched their selectivity preferences in Trial 2 (Fig. 3H).

To investigate the time course of this cell-level instability, we repeated this multi-trial EZM with an ITI of 1 h (Fig. 3N). Remarkably, our results were similar to the 24 h ITI data, suggesting that these cells can change their stimulus-specific activation patterns across short time scales (Fig. 3N–R). Once again, population level VIP^{ACC} stimulus-selectivity was not significantly different across the 2 trials (Fig. 3O). Trial 1 closed-selective cells showed increased activity in the closed arm (36% increase, Fig. 3Q, left, green) and open-selective cells were less active in the closed arm (38% decrease, Fig. 3Q, left, pink). Trial 1 selective cells again showed no change in activity when animals explored each arm type during Trial 2 (Fig. 3Q, right) and 68% transitioned from selective to neutral in Trial 2 (Fig. 3R). Additionally, 16% of all selective cells switched their selectivity preference in Trial 2 (Fig. 3R). Importantly, there was no difference between the percentage of stable cells when comparing the 24 h to the 1 h interval (*t* test, Mann–Whitney post test, $p = 0.7835$), suggesting that previously selective cells rapidly changed preferences (Fig. 3H and R).

For both 24 h and 1 h ITI EZM, the average Ca^{2+} activity of cells identified as selective or neutral in Trials 1 (Fig. 3I, J, S, T) or 2 (Fig. 3K, L, U, V) was compared across trials and no differences were found, showing that our results were not an effect of major shifts in activity levels or bleaching. There was also no significant difference in overall VIP^{ACC} activity (Fig. 3M, W) or in the percentage of time animals spent in the open arm in Trials 1 or 2 (Fig. 3D, P). These control analyses show that the neural differences found across trials did not result from differences in overall VIP^{ACC} activity or behavior. We also monitored Ca^{2+} activity over two different anxiety related assays (EZM and OF) and found that most EZM-selective cells were neutral in the OF, rather than selective for each anxiogenic zone across tasks (Fig. S5A–D). In addition, we used two variations of the standard EZM task, which could alter the aversiveness of the arena by changing the light intensity and increasing the height of the platform (Fig. S5E and H). We hypothesized that if open-selective cells encoded anxiety stably, their average activity in EZM variations with increased/decreased aversiveness should be higher/lower. There was no significant difference in the average Ca^{2+} activity of open-elective cells when comparing the Normal EZM to the Platform EZM (Fig. S5F, G) or the Dim Light EZM (Fig. S5I–K), even though animals explored the open arm more in the Dim Light EZM

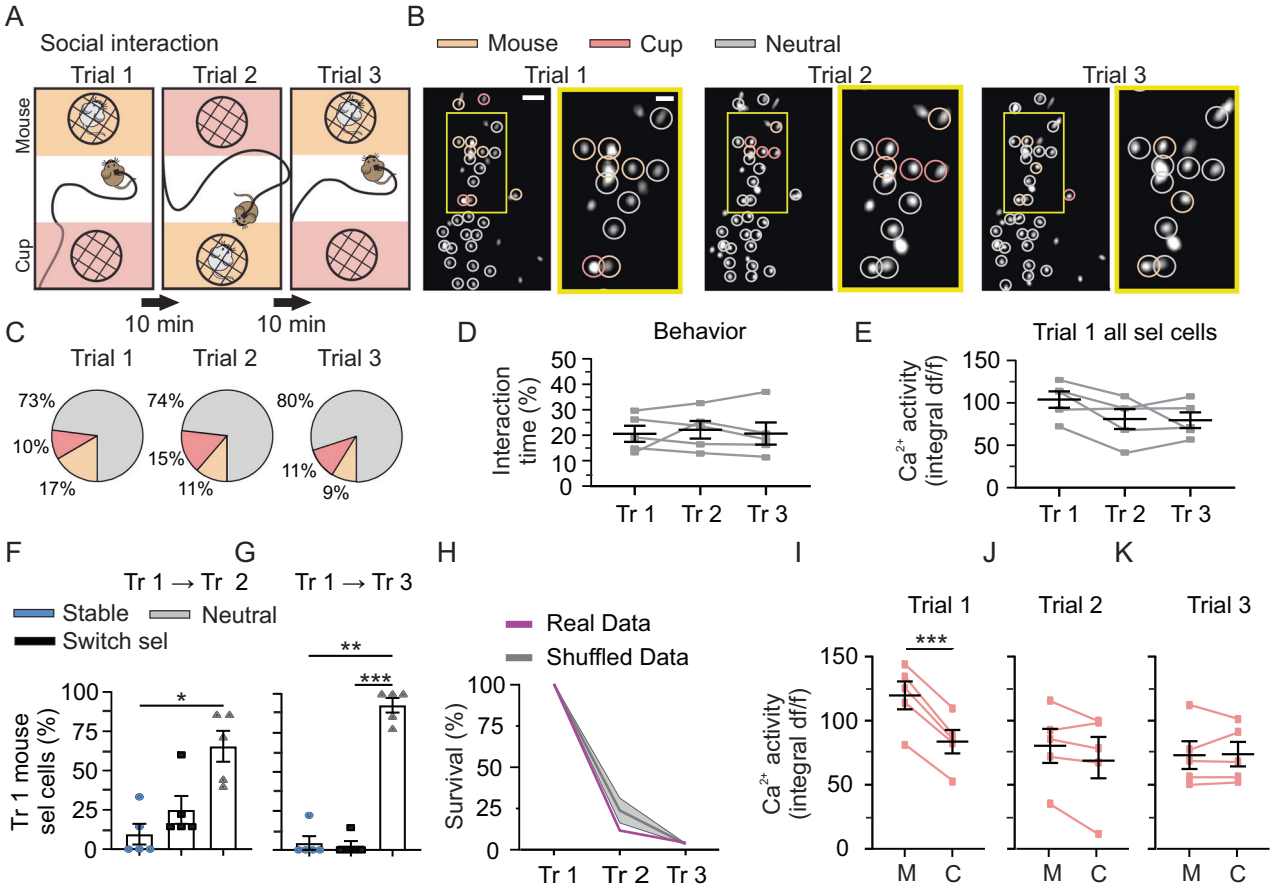

Fig. 4 Highly unstable VIP^{ACC} representations over multiple trials during a sociability task. A–K Multi-trial Sociability task. Animals explored an arena with an empty cup and a cup containing a novel mouse over 3 trials with 10 min ITIs. Data were registered to identify the same neurons in Trials 1–3. $N = 5$ mice, $n = 203$ cells. Trial duration = 5 min. **A** Schematic showing behavioral pipeline for multi-trial Sociability. Pink: empty cup zone, orange: novel mouse zone, white: neutral zone. **B** Images of VIP^{ACC} expressing GCaMP6f (white) in vivo during Trials 1–3 (left, middle, and right, respectively). The same cells were identified in all trials. Second, fourth, and sixth images are zoomed versions of the yellow boxed regions. Pink circles: cup-selective, orange circles: mouse-selective, gray circles: neutral cells. Scale bar = 85 μm in first, third, and fifth images, 30 μm in second, fourth, and sixth images. **C** In each Trial, VIP^{ACC} were classified as mouse-selective (orange, 17% in Trial 1, 11% in Trial 2, and 9% in Trial 3), cup-selective (pink, 10%, 15%, 11%), or neutral (gray, 73%, 74%, 80%). % of functional subtypes did not significantly change across trials. Two-way Repeated measures ANOVA. Selectivity: $F_{(2,12)} = 374.7$. $^{****}p < 0.0001$. Trial x Selectivity: $F_{(4,24)} = 1.516$. $p = 0.2291$. **D** % of time interacting with mouse cup. Repeated measures ANOVA $F_{(1.497,5.987)} = 0.2268$. $p = 0.7434$. **E** Using cells classified as selective in Trial 1, average Ca^{2+} activity was quantified in each trial. Repeated measures ANOVA. $F_{(1.532,6.130)} = 3.493$. $p = 0.1027$. % of cells identified as mouse-selective in Trial 1 that were stable, switched selectivity, or were neutral in Trials 2 (**F**) or 3 (**G**). **F** Trial 1 vs. Trial 2. Repeated measures One-way ANOVA. $F_{(1.682,6.724)} = 7.609$. $^{*}p = 0.0211$. Stable vs. Switched, $p = 0.4758$. Stable vs. Neutral, $^{*}p = 0.0365$. Switched vs. Neutral, $p = 0.1668$. **G** Trial 1 vs. Trial 3. Repeated measures ANOVA. $F_{(1.588,6.353)} = 106.9$. $^{****}p < 0.0001$. Stable vs. Switched, $p = 0.9607$. Stable vs. Neutral, $^{**}p = 0.0011$. Switched vs. Neutral, $^{***}p = 0.0003$. **H** Survival curve showing cells identified as mouse-selective in Trial 1 and the % of those cells that remained mouse-selective in Trials 2 and 3. Magenta: real data, gray: shuffled control data with SD. **I–K** For cells that were classified as mouse-selective in Trial 1, average Ca^{2+} activity during interactions with the mouse and empty cups was quantified in each trial. **I** Trial 1. Mouse vs. Cup. $^{***}p = 0.0003$. **J** Trial 2. Mouse vs. Cup. $p = 0.1421$. **K** Trial 3. Mouse vs. Cup. $p = 0.8520$.

(Fig. S5L). These multi-trial experiments show that although VIP^{ACC} stimulus-selectivity is stable within a given trial (Fig. 1, Fig. S1W), stimulus-selectivity is highly unstable over rapid timescales in a variety of anxiety-related assays.

Rapid changes in VIP^{ACC} stimulus-selectivity in social and object interaction tasks

Next, we investigated whether VIP^{ACC} instability was unique to anxiety-related assays, or a feature of these cells across social and object interaction tasks. To capture the precise dynamics of this instability, we designed these experiments to assess instability over trials with very brief ITIs. In the multi-trial Social Interaction assay, animals explored an arena with two mesh wire cups (one empty and one housing a novel mouse) over 3 trials (5 min trials, 10 min ITI) (Fig. 4A). The same stimulus mouse was used for all 3 trials and its location within the chamber was alternated. Cells were registered and their selectivity was calculated in each trial (Fig. 4B, C). Percentages of each cell type were not significantly different across all 3 trials (mouse-selective: 17%, 11%, 9%, cup-selective: 10%, 15%, 11%, neutral: 73%, 74%, 80%), suggesting that the population encoding did not change across trials (Fig. 4C). Additionally, the behavior (Fig. 4D) and average Ca^{2+} activity of all selective cells (Fig. 4E) remained constant across all trials, suggesting that mice remained interested in investigating the stimulus mouse across trials and activity was not modulated by repeated exposure to a stimulus. Much like the multi-trial EZM data, VIP^{ACC} encoding was highly and rapidly unstable at the individual cell level (Fig. 4B and F–K). Few Trial 1 mouse-selective cells remained selective in other trials and this percentage of stable cells was no higher than expected by chance (based on shuffled data, Fig. 4H). Lastly, we found that Trial 1 mouse-selective cells that showed increased activity during interactions

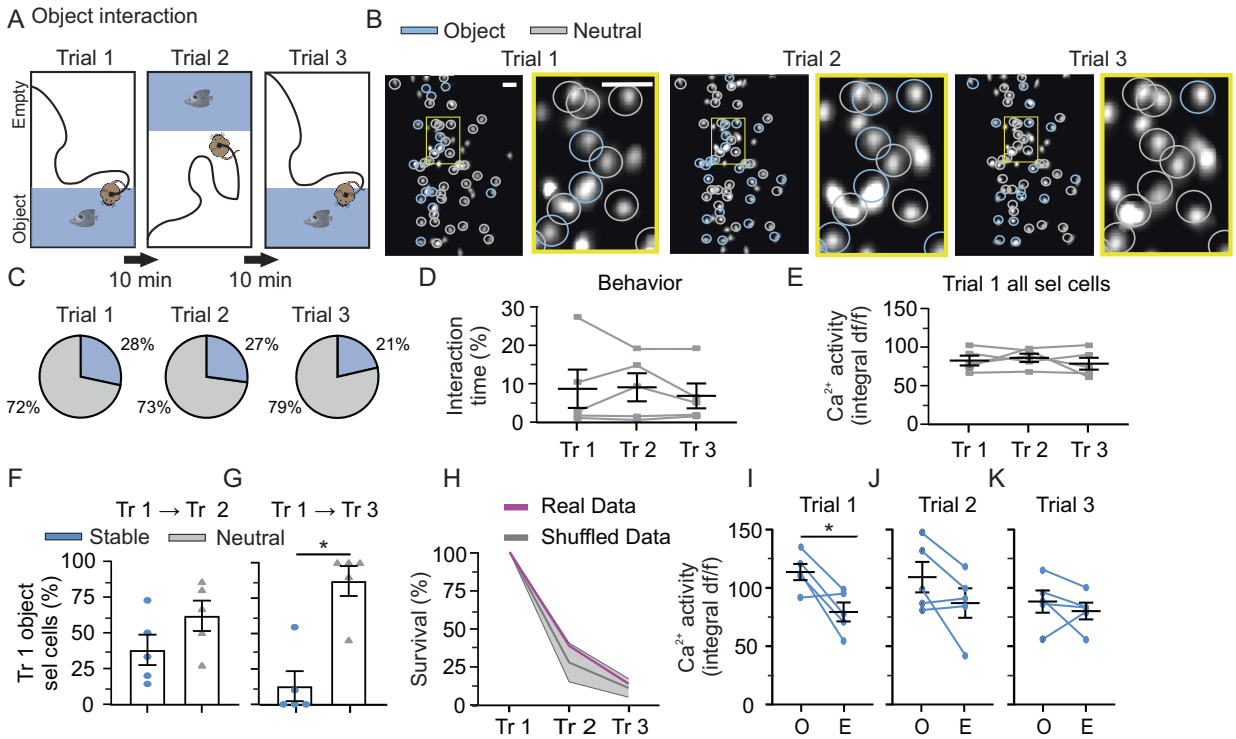

Fig. 5 Highly unstable VIP^{ACC} representations over multiple trials during an object interaction task. A–K Multi-trial Object Interaction task. Animals explored an arena with a novel object over 3 trials with 10 min ITIs. Data were registered to identify the same neurons in Trials 1–3. $N = 5$ mice, $n = 162$ cells. Trial duration = 5 min. **A** Schematic showing behavioral pipeline for multi-trial Object task. Blue: novel object zone, white: neutral zone. **B** Images of VIP^{ACC} expressing GCaMP6f (white) in vivo during Trials 1–3 (left, middle, and right, respectively). The same cells were identified in all trials. Second, fourth, and sixth images are zoomed versions of the yellow boxed regions. Blue circles: object-selective, gray circles: neutral cells. Scale bar = 30 μm in first, third, and fifth images, 45 μm in second, fourth, and sixth images. **C** In each Trial, VIP^{ACC} were classified as cup-selective (blue, 28% in Trial 1, 27% in Trial 2, and 21% in Trial 3) or neutral (72%, 73%, 79%). Percentages of functional subtypes did not change across trials. Two-way Repeated measures ANOVA. Selectivity: $F_{(1,8)} = 18.77$. $^{**}p = 0.0025$. Trial x Selectivity: $F_{(2,16)} = 1.261$. $p = 0.3101$. **D** % time interacting with novel object. Repeated measures ANOVA. $F_{(1.642,6.567)} = 0.6484$. $p = 0.5244$. **E** Using cells classified as selective in Trial 1, average Ca^{2+} activity was quantified in each trial. Repeated measures ANOVA. $F_{(1.364,5.454)} = 0.3859$. $p = 0.6227$. % of cells identified as object-selective in Trial 1 that were stable, switched selectivity, or were neutral in Trials 2 (**F**) or 3 (**G**). **F** Trials 1 and 2. Stable vs. Neutral. $p = 0.3243$. **G** Trials 1 and 3. Stable vs. Neutral. $^{*}p = 0.0248$. **H** Survival curve showing cells identified as object-selective in Trial 1 and the % of those cells that remained object-selective in Trials 2 and 3. Magenta: real data, gray: shuffled control data with SD. **I–K** For cells that were classified as object-selective in Trial 1, average Ca^{2+} activity during interactions with the object or exploration of the empty zone was quantified in each trial. **I** Trial 1. Object vs. Empty. $^{*}p = 0.0274$. **J** Trial 2. Object vs. Empty. $p = 0.1291$. **K** Trial 3. Object vs. Empty. $p = 0.4231$. All images are representative. Each replicate represents one mouse. All statistics performed with Paired *t* test unless otherwise noted. ITI inter-trial interval, Tr Trial, df/f Deltaf/f, Sel selective, O object, E empty.

with the mouse, rather than the cup, in Trial 1 (30% increase, Fig. 4I), showed no link between their activity and behavior in Trials 2 and 3 (Fig. 4J, K). It is possible that if VIP^{ACC} encode social and spatial information, that the instability in stimulus preference could have resulted from alternating the location of the stimulus mouse between trials [63]. However, this is unlikely because the stimulus mouse was in the same position for Trials 1 and 3 and Trial 1 selective cells did not recover their original stimulus preferences in Trial 3.

To investigate VIP^{ACC} instability during interactions with objects, we used a multi-trial Object Interaction assay (Fig. 5A). Animals explored a rectangular arena with one empty side and one side that contained a novel object (Fig. 5A). There were 3 trials (5 min trials, 10 min ITI) and the same object was used for all trials. Cells were registered and identified as object-selective or neutral (Fig. 5B, C). There was no significant difference in the percentage of cells that were object-selective or neutral in each trial (object-selective: 28%, 27%, 21%, neutral: 72%, 73%, 79%, Fig. 5C). There were no differences in time spent interacting with the object (Fig. 5D) or average Ca^{2+} activity of selective cells (Fig. 5E) across trials. These data suggest population-level stability and that repetitive exposure to the object did not change the animal's interest in interacting with it. In 4 out of 5 mice, the majority of selective cells became neutral in Trial 2 (Fig. 5F), and in Trial 3, even more cells transitioned to neutral (Neutral vs. stable, 6.7-fold difference, Fig. 5G). The small number of stable cells in Trial 3 was no higher than expected by chance (Fig. 5H). Additionally, trial 1 selective cells (Fig. 5I) did not show significantly different activity during object interactions in Trials 2 or 3 (Fig. 5J, K). Taken together, these Ca^{2+} imaging experiments demonstrate that individual VIP^{ACC} can encode anxiety-related, social, or non-social stimuli within a given trial, but these representations are highly unstable over multiple trials. In addition, our results show that population-level VIP^{ACC} encoding may remain stable, even when cell-level encoding is rapidly changing.

Brain-wide maps of synaptic input to ACC interneurons

We also aimed to determine whether VIP^{ACC} receive projections from other brain areas involved in anxiety and social behavior. To achieve this and assess the diversity of inputs to different ACC interneuron types, we used rabies virus-mediated trans-synaptic mapping (Fig. S6A–M, and see negative controls in Fig. S7). Starter cells in the ACC for VIP, somatostatin (SST^{ACC}), or parvalbumin (PV^{ACC}) were distributed throughout cortical layers (Fig. S6E). Input neurons were quantified for the top 2 quartiles of labeled brain regions with the most input cells for each cell type (Fig. S6G-M).

For VIP^{ACC}, retrogradely-labeled neurons were most prominent in primary and associative cortical areas (prim/asso, 34% of top 2 quartile retrogradely-labeled neurons), PFC, thalamic nuclei, and the medial septal complex (MSC), suggesting that these regions were highly connected to VIP^{ACC} (Fig. S6G). We partitioned these brain areas into subregions and determined that VIP^{ACC} received extensive connections from the contralateral ACC (cl-ACC, 31% of top 2 quartile retrogradely-labeled neurons, Fig. S6I), prelimbic cortex (PrL, 50% of top 2 quartile retrogradely-labeled PFC neurons, Fig. S6H, K), retrosplenial cortex (RSC, 86% of top 2 quartile retrogradely-labeled prim/asso neurons, Fig. S6H, J, L), and anteromedial thalamic nucleus (AM, 46% of top 2 quartile retrogradely-labeled thalamic neurons, Fig. S6H, M). Top input regions were also identified for SST^{ACC} and PV^{ACC} to map connectivity for each interneuron subtype within the ACC. For all 3 cell types, prim/asso was the top region (Fig. S6G) and numerous input areas were identified (Fig. S6G-M).

We additionally used ex vivo electrophysiology to assess whether the connections found in these rabies tracing datasets could be functional (Fig. S6N-P). We focused on one of the most extensive connections: RSC to VIP^{ACC}. By injecting a virus that expresses channelrhodopsin-2 (ChR2) in the RSC of a genetic mouse line that expresses EGFP in VIP cells, we optogenetically stimulated RSC axons in the ACC and recorded from VIP^{ACC} in acute brain slices (Fig. S6N-O). We found that this connection is indeed functional across layers of the ACC, with the highest connectivity to L2 VIP^{ACC} (Fig. S6P). Overall, our connectivity data showed that VIP^{ACC} receive long-range projections from regions implicated in emotional regulation, social cognitive behavior, memory formation, and motor actions.

DISCUSSION

Multimodal inhibitory circuits in the ACC

The ACC is implicated in a wide range of behavioral functions. Our work supports past findings by connecting ACC activity with anxiety-related and social behaviors and identifies a possible neural substrate for processing multimodal stimuli. Additionally, some VIP^{ACC} encoded interactions with objects, which corresponds with past characterizations of neural correlates in the ACC for object recognition and memory [14, 15]. However, an important facet of our finding is the diverse range of neuronal representations encoded by individual VIP^{ACC}, which point to the varied roles of the ACC.

Human imaging studies have shown that ACC activity increases as individuals perform social and emotional tasks, as compared to non-social tasks [64]. Interestingly, these data demonstrate heterogeneous activation of ACC subregions, where the perigenual and rostral ACC are implicated in social tasks and dorsal ACC is selectively active during non-social cognitive tasks [64]. Our lenses were located at the border of the ventral and dorsal ACC subregions (A24a and A24b [61, 65]). Future research could monitor VIP cells in different ACC subregions to determine whether the selectivity distributions differ. One caveat of our study is that implanting lenses damaged the surrounding tissue in the ACC and to image this area, we extracted other brain regions, including M2. Nevertheless, our data demonstrated that implanted animals had no locomotor impairments or abnormal behaviors in the EZM or social tasks.

Using LR analysis, we found that the statistical model's decoding performance improved as more stimulus-selective VIP^{ACC} were included in the training, suggesting that groups of VIP interneurons could work cooperatively to perform a function. Electrical coupling has been observed within VIP inhibitory networks [21, 66] and VIP cells can also disinhibit members of their own population, leading to increased co-activation, which may allow these subnetworks to encode stimuli cooperatively and amplify the population output [21]. Although the ROC analysis showed that neutral cells did not preferentially activate to specific stimuli, the LR analysis demonstrated that they can still be used to decode behavior (although with worse performance than selective cells). A point of consideration in our analysis, is that we set a strict threshold for classifying a cell as selective, so cells designated as neutral may still carry weak stimulus-related information.

Although our approach identified VIP^{ACC} with clear stimulus preferences, the function of this interneuron type during anxiogenic environments and social interactions may be more complex than simply encoding specific stimuli. For example, recordings in the rodent PFC and ACC during various tasks and learning paradigms have demonstrated that the activity of some neurons correlates to higher-order processes related to cognitive function, including learning rules, generalization, effort, and goal-directed behavior [2, 5, 6, 13, 14, 67–77]. Additionally, an open-selective cell, for example, may not necessarily encode the aversiveness of the environment, but other sensorimotor or affective aspects that are associated with the behavior. Murugan et al. [63] identified nucleus accumbens-projecting prelimbic neurons that were active during social investigation, but only in specific spatial locations. Stimulus location is unlikely to explain our data because, during the multi-trial tasks, placing the stimulus in its original location did not preferentially engage or reactivate previously identified selective cells. Although we demonstrate that VIP cell activity can encode behavior, more studies will be needed to determine whether manipulating VIP activity is sufficient to cause changes in behavior.

Heterogeneous inhibitory subcircuits in the ACC

Our data showed that VIP^{ACC} are engaged by diverse stimuli, but do not activate as one uniform group. This may be a result of differential synaptic targeting of subgroups of VIP^{ACC} by long-range inputs or differential neuromodulator receptor expression. VIP interneurons express a variety of neuromodulator receptors, which may modulate VIP^{ACC} activity and thereby exert context-dependent disinhibition [19, 22, 78–81]. Moreover, our data show that only a subgroup of VIP cells is targeted by RSC inputs. Through the actions of neuromodulators [22, 27, 30] and synaptic inputs on subgroups of VIP^{ACC}, these cells may recruit subpopulations of Pyr cells that are behaviorally relevant or encode specific information.

We demonstrated that some VIP^{ACC} are engaged by social and object novelty. Locus coeruleus neurons are the primary source of norepinephrine in the forebrain and are recruited by novel stimuli [82–84]. In the cortex, norepinephrine differentially regulates the activity of interneurons [85, 86], but it remains to be shown whether differential recruitment of VIP^{ACC} by novel stimuli is dependent on norepinephrine.

Although VIP interneurons primarily synapse onto other inhibitory cells, disinhibiting excitatory Pyr cells, some subpopulations form direct connections with Pyr cells [18, 27, 87]. VIP^{ACC} that either inhibit or disinhibit Pyr cells are likely to have different functionalities. Therefore, it would be important to see whether these subpopulations exhibit different stimulus preferences. Because VIP interneurons can modulate the activity of Pyr, SST, and PV cells, future work could investigate whether these other cells types demonstrate heterogeneity and instability at the cellular level in the ACC. Recent transcriptomic data showed that VIP interneurons can be subdivided into over 20 groups with a wide range of genetic profiles [32, 33, 78]. Some VIP cells express the molecular markers ChAT, CCK, or CR, which have been linked to differences in morphology or electrophysiological patterns [24, 27, 34, 88]. Molecular heterogeneity of CCK and CR markers did not correlate with EZM-associated c-Fos levels, however. One caveat in this experiment is that c-Fos may not provide enough temporal sensitivity to identify subtle differences across VIP subtypes. Additionally, our data show no relationship between the cortical depth of interneuron soma and their stimulus

selectivity in the EZM. Together with our results that showed VIP^{ACC} representations across trials were highly unstable, these findings suggest that at a given time, a specific stimulus is represented by a mixed population of VIP^{ACC} subtypes.

Unstable representations in cortical function

To our knowledge, these data provide the first evidence that VIP^{ACC} encoding is highly unstable over time. Prior work has characterized Pyr cell instability in the hippocampus and several cortical areas, but has not elucidated whether different types of interneurons exhibit instability in their encoding [36, 37, 39, 40]. Importantly, our data recapitulate some of the findings in Pyr cells in other brain regions, such as population-wide stability [37, 40, 89–92]. An important difference is that while most studies have shown subtle shifts in tuning over days [93–96], our data shows that representations in VIP^{ACC} are highly unstable, rapidly shifting over tens of minutes. In the hippocampus, rapid changes have been observed in the representation of place cells upon repeated exposure to the same environment [97, 98]. In this regard, VIP interneurons in the ACC share similarities with these hippocampal cell types. Peters et al. [95] demonstrated that the relationship between neuronal activity in the motor cortex and motor movements becomes more consistent with learning. Although, the mice in our study did not perform a learned task, we did not find any evidence that the representation of individual ACC interneurons became more stable with repetitive exposure to the same stimuli (EZM tasks, and social and non-social interactions).

In the EZM task, we found that the stability of neuronal representations shifted in a time-dependent manner with interneurons recorded at shorter intervals exhibiting a higher degree of stability. It is possible that the almost complete turnover in neuronal representations observed at longer time scales is due to a lack of memory consolidation [99]. Therefore, future studies could decipher how the stability of interneuronal representations changes as a mouse learns a cognitive task or during fear memory formation [22, 59]. An alternative explanation is that computations performed by VIP cells in the ACC require an unstable population of interneurons. For example, in the motor cortex, neuronal representations exist in a redundant network, where they fluctuate without affecting the overall behavior [100].

Unstable representations have been hypothesized to be an adaptive feature of healthy neural function by increasing the system's flexibility and redundancy [41, 101]. These features may make the brain more resilient by allowing for normal behavioral function, even in the face of damage or change to individual cells [41]. Modeling approaches also suggests that this instability contributes to efficient coding by neuronal networks and may underlie cellular mechanisms important for learning and memory [38, 101]. Turnover and change are accepted as fundamental processes for synaptic function [102–104], and it has been hypothesized that turnover in the stimulus-related activity of individual neurons may be equally important [38, 41]. Our results also suggest that the representations in VIP cells are unlikely to be defined by the relatively hard-wired connectivity patterns alone, since these change on a slower timescale. Therefore, activity-dependent mapping alone would not suffice to understand the sources of the observed variability and instability of VIP cells in our datasets. Therefore, our data suggest, that the instability in VIP cells is encoded not only by connectivity, but also by encoding instability in the upstream brain areas themselves.

Using in vivo imaging with cellular resolution in freely behaving mice, we demonstrated that VIP^{ACC} are functionally heterogeneous, where individual cells encode for diverse stimuli within a given behavioral trial. ROC analysis identified stimulus-selective VIP^{ACC} that encoded anxiety-related contexts, interactions with mice and objects, and novelty, even when the population activity of VIP^{ACC} was not biased towards a particular stimulus. Additionally, our statistical model suggests that VIP^{ACC} can work cooperatively to encode behavior. Lastly, we found that stimulus-selectivity at the level of the individual neuron was highly and rapidly unstable over multiple trials, even when the whole VIP^{ACC} population representations remained stable. To our knowledge, these data provide the first evidence of functional heterogeneity and instability of VIP^{ACC} in vivo, which provides a framework for how the ACC encodes information across diverse behavioral states.

DATA AVAILABILITY

All relevant data are within the paper, and underlying data are available at https://github.com/CruzMartinLab. Custom-written routines for behavioral tracking, Ca^{2+} imaging analysis, and miniscope models and tools are available at https://github.com/CruzMartinLab. For further information, please contact the corresponding author.

REFERENCES

1. Etkin A, Egner T, Peraza DM, Kandel ER, Hirsch J. Resolving emotional conflict: a role for the rostral anterior cingulate cortex in modulating activity in the amygdala. Neuron. 2006;51:871–82.
2. Kennerley SW, Walton ME, Behrens TE, Buckley MJ, Rushworth MF. Optimal decision making and the anterior cingulate cortex. Nat Neurosci. 2006;9:940–7.
3. Lieberman MD, Eisenberger NI. The dorsal anterior cingulate cortex is selective for pain: Results from large-scale reverse inference. Proc Natl Acad Sci USA. 2015;112:15250–5.
4. Marusak HA, Thomason ME, Peters C, Zundel C, Elrahal F, Rabinak CA. You say 'prefrontal cortex' and I say 'anterior cingulate': meta-analysis of spatial overlap in amygdala-to-prefrontal connectivity and internalizing symptomology. Transl Psychiatry. 2016;6:e944.
5. Rolls ET. The cingulate cortex and limbic systems for action, emotion, and memory. Handb Clin Neurol. 2019;166:23–37.
6. Brockett AT, Tennyson SS, deBettencourt CA, Gaye F, Roesch MR. Anterior cingulate cortex is necessary for adaptation of action plans. Proc Natl Acad Sci USA. 2020;117:6196–204.
7. Nitschke JB, Sarinopoulos I, Oathes DJ, Johnstone T, Whalen PJ, Davidson RJ, et al. Anticipatory activation in the amygdala and anterior cingulate in generalized anxiety disorder and prediction of treatment response. Am J Psychiatry. 2009;166:302–10.
8. Guo B, Chen J, Chen Q, Ren K, Feng D, Mao H, et al. Anterior cingulate cortex dysfunction underlies social deficits in Shank3 mutant mice. Nat Neurosci. 2019;22:1223–34.
9. Rudebeck PH, Buckley MJ, Walton ME, Rushworth MF. A role for the macaque anterior cingulate gyrus in social valuation. Science 2006;313:1310–2.
10. Rudebeck PH, Putnam PT, Daniels TE, Yang T, Mitz AR, Rhodes SE, et al. A role for primate subgenual cingulate cortex in sustaining autonomic arousal. Proc Natl Acad Sci USA. 2014;111:5391–6.
11. Weible AP, Piscopo DM, Rothbart MK, Posner MI, Niell CM. Rhythmic brain stimulation reduces anxiety-related behavior in a mouse model based on meditation training. Proc Natl Acad Sci USA. 2017;114:2532–7.
12. Kim SS, Wang H, Li XY, Chen T, Mercaldo V, Descalzi G, et al. Neurabin in the anterior cingulate cortex regulates anxiety-like behavior in adult mice. Mol Brain. 2011;4:6.
13. Totah NK, Kim YB, Homayoun H, Moghaddam B. Anterior cingulate neurons represent errors and preparatory attention within the same behavioral sequence. J Neurosci. 2009;29:6418–26.
14. Weible AP, Rowland DC, Monaghan CK, Wolfgang NT, Kentros CG. Neural correlates of long-term object memory in the mouse anterior cingulate cortex. J Neurosci. 2012;32:5598–608.
15. Weible AP, Rowland DC, Pang R, Kentros C. Neural correlates of novel object and novel location recognition behavior in the mouse anterior cingulate cortex. J Neurophysiol. 2009;102:2055–68.
16. Xiao Z, Martinez E, Kulkarni PM, Zhang Q, Hou Q, Rosenberg D, et al. Cortical Pain Processing in the Rat Anterior Cingulate Cortex and Primary Somatosensory Cortex. Front Cell Neurosci. 2019;13:165.
17. Askew CE, Lopez AJ, Wood MA, Metherate R. Nicotine excites VIP interneurons to disinhibit pyramidal neurons in auditory cortex. Synapse. 2019;73:e22116.
18. Lee S, Kruglikov I, Huang ZJ, Fishell G, Rudy B. A disinhibitory circuit mediates motor integration in the somatosensory cortex. Nat Neurosci. 2013;16:1662–70.
19. Pi HJ, Hangya B, Kvitsiani D, Sanders JI, Huang ZJ, Kepecs A. Cortical interneurons that specialize in disinhibitory control. Nature. 2013;503:521–4.

20. Karnani MM, Jackson J, Ayzenshtat I, Hamzehei Sichani A, Manoocheri K, Kim S, et al. Opening Holes in the Blanket of Inhibition: Localized Lateral Disinhibition by VIP Interneurons. J Neurosci. 2016;36:3471–80.
21. Karnani MM, Jackson J, Ayzenshtat I, Tucciarone J, Manoocheri K, Snider WG, et al. Cooperative Subnetworks of Molecularly Similar Interneurons in Mouse Neocortex. Neuron. 2016;90:86–100.
22. Melzer S, Newmark ER, Mizuno GO, Hyun M, Philson AC, Quiroli E, et al. Bombesin-like peptide recruits disinhibitory cortical circuits and enhances fear memories. Cell 2021;184:5622–34. e25.
23. Wall NR, De La Parra M, Sorokin JM, Taniguchi H, Huang ZJ, Callaway EM. Brain-Wide Maps of Synaptic Input to Cortical Interneurons. J Neurosci. 2016;36:4000–9.
24. Ferezou I, Cauli B, Hill EL, Rossier J, Hamel E, Lambolez B. 5-HT3 receptors mediate serotonergic fast synaptic excitation of neocortical vasoactive intestinal peptide/cholecystokinin interneurons. J Neurosci. 2002;22:7389–97.
25. Poorthuis RB, Enke L, Letzkus JJ. Cholinergic circuit modulation through differential recruitment of neocortical interneuron types during behaviour. J Physiol. 2014;592:4155–64.
26. Pronneke A, Witte M, Mock M, Staiger JF. Neuromodulation Leads to a Burst-Tonic Switch in a Subset of VIP Neurons in Mouse Primary Somatosensory (Barrel) Cortex. Cereb Cortex. 2020;30:488–504.
27. Obermayer J, Luchicchi A, Heistek TS, de Kloet SF, Terra H, Bruinsma B, et al. Prefrontal cortical ChAT-VIP interneurons provide local excitation by cholinergic synaptic transmission and control attention. Nat Commun. 2019;10:5280.
28. Granger AJ, Wang W, Robertson K, El-Rifai M, Zanello AF, Bistrong K, et al. Cortical ChAT(+) neurons co-transmit acetylcholine and GABA in a target- and brain-region-specific manner. Elife. 2020;9.
29. Garrett M, Manavi S, Roll K, Ollerenshaw DR, Groblewski PA, Ponvert ND, et al. Experience shapes activity dynamics and stimulus coding of VIP inhibitory cells. Elife. 2020;9.
30. Turi GF, Li WK, Chavlis S, Pandi I, O'Hare J, Priestley JB, et al. Vasoactive intestinal polypeptide-expressing interneurons in the hippocampus support goal-oriented spatial learning. Neuron. 2019;101:1150–65. e8.
31. Lee AT, Cunniff MM, See JZ, Wilke SA, Luongo FJ, Ellwood IT, et al. VIP interneurons contribute to avoidance behavior by regulating information flow across hippocampal-prefrontal networks. Neuron. 2019;102:1223–34. e4.
32. Tasic B, Yao Z, Graybuck LT, Smith KA, Nguyen TN, Bertagnolli D, et al. Shared and distinct transcriptomic cell types across neocortical areas. Nature. 2018;563:72–8.
33. Tasic B. Single cell transcriptomics in neuroscience: cell classification and beyond. Curr Opin Neurobiol. 2018;50:242–9.
34. Gonchar Y, Wang Q, Burkhalter A. Multiple distinct subtypes of GABAergic neurons in mouse visual cortex identified by triple immunostaining. Front Neuroanat. 2007;1:3.
35. Tremblay R, Lee S, Rudy B. GABAergic Interneurons in the Neocortex: From Cellular Properties to Circuits. Neuron. 2016;91:260–92.
36. Liberti WA 3rd, Markowitz JE, Perkins LN, Liberti DC, Leman DP, Guitchounts G, et al. Unstable neurons underlie a stable learned behavior. Nat Neurosci. 2016;19:1665–71.
37. Rule ME, Loback AR, Raman DV, Driscoll LN, Harvey CD, O'Leary T Stable task information from an unstable neural population. Elife. 2020;9.
38. Rule ME, O'Leary T, Harvey CD. Causes and consequences of representational drift. Curr Opin Neurobiol. 2019;58:141–7.
39. Levy SJ, Kinsky NR, Mau W, Sullivan DW, Hasselmo ME. Hippocampal spatial memory representations in mice are heterogeneously stable. Hippocampus. 2021;31:244–60.
40. Driscoll LN, Pettit NL, Minderer M, Chettih SN, Harvey CD. Dynamic Reorganization of Neuronal Activity Patterns in Parietal Cortex. Cell. 2017;170:986–99. e16.
41. Chambers AR, Rumpel S. A stable brain from unstable components: Emerging concepts and implications for neural computation. Neuroscience. 2017;357:172–84.
42. Liberti WA, Perkins LN, Leman DP, Gardner TJ. An open source, wireless capable miniature microscope system. J Neural Eng. 2017;14:045001.
43. Taniguchi H, He M, Wu P, Kim S, Paik R, Sugino K, et al. A resource of Cre driver lines for genetic targeting of GABAergic neurons in cerebral cortex. Neuron. 2011;71:995–1013.
44. Hippenmeyer S, Vrieseling E, Sigrist M, Portmann T, Laengle C, Ladle DR, et al. A developmental switch in the response of DRG neurons to ETS transcription factor signaling. PLoS Biol. 2005;3:e159.
45. He M, Tucciarone J, Lee S, Nigro MJ, Kim Y, Levine JM, et al. Strategies and tools for combinatorial targeting of GABAergic neurons in mouse cerebral cortex. Neuron. 2016;92:555.
46. Oh SW, Harris JA, Ng L, Winslow B, Cain N, Mihalas S, et al. A mesoscale connectome of the mouse brain. Nature. 2014;508:207–14.
47. Kohara K, Pignatelli M, Rivest AJ, Jung HY, Kitamura T, Suh J, et al. Cell type-specific genetic and optogenetic tools reveal hippocampal CA2 circuits. Nat Neurosci. 2014;17:269–79.
48. Haubensak W, Kunwar PS, Cai H, Ciocchi S, Wall NR, Ponnusamy R, et al. Genetic dissection of an amygdala microcircuit that gates conditioned fear. Nature 2010;468:270–6.
49. Ghosh KK, Burns LD, Cocker ED, Nimmerjahn A, Ziv Y, Gamal AE, et al. Miniaturized integration of a fluorescence microscope. Nat Methods. 2011;8:871–8.
50. Aharoni D, Khakh BS, Silva AJ, Golshani P. All the light that we can see: a new era in miniaturized microscopy. Nat Methods. 2019;16:11–3.
51. Comer AL, Sriram B, Yen WW, Cruz-Martin A A Pipeline using bilateral in utero electroporation to interrogate genetic influences on rodent behavior. J Vis Exp. 2020.
52. Mathis A, Mamidanna P, Cury KM, Abe T, Murthy VN, Mathis MW, et al. DeepLabCut: markerless pose estimation of user-defined body parts with deep learning. Nat Neurosci. 2018;21:1281–9.
53. Comer AL, Jinadasa T, Sriram B, Phadke RA, Kretsge LN, Nguyen TPH, et al. Increased expression of schizophrenia-associated gene C4 leads to hypoconnectivity of prefrontal cortex and reduced social interaction. PLoS Biol. 2020;18:e3000604.
54. Giovannucci A, Friedrich J, Gunn P, Kalfon J, Brown BL, Koay SA, et al. CaImAn an open source tool for scalable calcium imaging data analysis. Elife. 2019;8.
55. Virtanen P, Gommers R, Oliphant TE, Haberland M, Reddy T, Cournapeau D, et al. SciPy 1.0: fundamental algorithms for scientific computing in Python. Nat Methods. 2020;17:261–72.
56. Jimenez JC, Su K, Goldberg AR, Luna VM, Biane JS, Ordek G, et al. Anxiety cells in a hippocampal-hypothalamic circuit. Neuron. 2018;97:670–83. e6.
57. Li Y, Mathis A, Grewe BF, Osterhout JA, Ahanonu B, Schnitzer MJ, et al. Neuronal representation of social information in the medial amygdala of awake behaving mice. Cell. 2017;171:1176–90. e17.
58. Kingsbury L, Huang S, Raam T, Ye LS, Wei D, Hu RK, et al. Cortical representations of conspecific sex shape social behavior. Neuron. 2020;107:941–53. e7.
59. Sriram B, Li L, Cruz-Martin A, Ghosh A. A sparse probabilistic code underlies the limits of behavioral discrimination. Cereb Cortex. 2020;30:1040–55.
60. Lein ES, Hawrylycz MJ, Ao N, Ayres M, Bensinger A, Bernard A, et al. Genome-wide atlas of gene expression in the adult mouse brain. Nature. 2007;445:168–76.
61. Paxinos F The mouse brain in stereotaxic coordinates, 4th Edition. 2012.
62. Callaway EM, Luo L. Monosynaptic circuit tracing with glycoprotein-deleted rabies viruses. J Neurosci. 2015;35:8979–85.
63. Murugan M, Jang HJ, Park M, Miller EM, Cox J, Taliaferro JP, et al. Combined social and spatial coding in a descending projection from the prefrontal cortex. Cell. 2017;171:1663–77. e16.
64. Di Martino A, Ross K, Uddin LQ, Sklar AB, Castellanos FX, Milham MP. Functional brain correlates of social and nonsocial processes in autism spectrum disorders: an activation likelihood estimation meta-analysis. Biol Psychiatry. 2009;65:63–74.
65. Fillinger C, Yalcin I, Barrot M, Veinante P. Afferents to anterior cingulate areas 24a and 24b and midcingulate areas 24a' and 24b' in the mouse. Brain Struct Funct. 2017;222:1509–32.
66. Galarreta M, Hestrin S. A network of fast-spiking cells in the neocortex connected by electrical synapses. Nature. 1999;402:72–5.
67. Tanimizu T, Kenney JW, Okano E, Kadoma K, Frankland PW, Kida S. Functional connectivity of multiple brain regions required for the consolidation of social recognition memory. J Neurosci. 2017;37:4103–16.
68. Hayden BY, Heilbronner SR, Pearson JM, Platt ML. Surprise signals in anterior cingulate cortex: neuronal encoding of unsigned reward prediction errors driving adjustment in behavior. J Neurosci. 2011;31:4178–87.
69. Hayden BY, Platt ML. Fool me once, shame on me–fool me twice, blame the ACC. Nat Neurosci. 2006;9:857–9.
70. Bush G, Luu P, Posner MI. Cognitive and emotional influences in anterior cingulate cortex. Trends Cogn Sci. 2000;4:215–22.
71. Porter BS, Hillman KL. Dorsomedial prefrontal neural ensembles reflect changes in task utility that culminate in task quitting. J Neurophysiol. 2021;126:313–29.
72. Porter BS, Li K, Hillman KL Regional activity in the rat anterior cingulate cortex and insula during persistence and quitting in a physical-effort task. eNeuro. 2020;7.
73. Carrillo M, Han Y, Migliorati F, Liu M, Gazzola V, Keysers C. Emotional mirror neurons in the rat's anterior cingulate cortex. Curr Biol. 2019;29:2104.
74. Porter BS, Hillman KL, Bilkey DK. Anterior cingulate cortex encoding of effortful behavior. J Neurophysiol. 2019;121:701–14.
75. Hillman KL, Bilkey DK. Persisting through subjective effort: a key role for the anterior cingulate cortex? Behav Brain Sci. 2013;36:691–2. discussion 707-26.
76. Hillman KL, Bilkey DK. Neurons in the rat anterior cingulate cortex dynamically encode cost-benefit in a spatial decision-making task. J Neurosci. 2010;30:7705–13.
77. Pearson JM, Hayden BY, Raghavachari S, Platt ML. Neurons in posterior cingulate cortex signal exploratory decisions in a dynamic multioption choice task. Curr Biol. 2009;19:1532–7.
78. Tasic B, Menon V, Nguyen TN, Kim TK, Jarsky T, Yao Z, et al. Adult mouse cortical cell taxonomy revealed by single cell transcriptomics. Nat Neurosci. 2016;19:335–46.

79. Zhang S, Xu M, Kamigaki T, Hoang Do JP, Chang WC, Jenvay S, et al. Selective attention. Long-range and local circuits for top-down modulation of visual cortex processing. Science. 2014;345:660–5.
80. Krabbe S, Paradiso E, d'Aquin S, Bitterman Y, Courtin J, Xu C, et al. Adaptive disinhibitory gating by VIP interneurons permits associative learning. Nat Neurosci. 2019;22:1834–43.
81. Letzkus JJ, Wolff SB, Luthi A. Disinhibition, a circuit mechanism for associative learning and memory. Neuron. 2015;88:264–76.
82. Berridge CW, Waterhouse BD. The locus coeruleus-noradrenergic system: modulation of behavioral state and state-dependent cognitive processes. Brain Res Brain Res Rev. 2003;42:33–84.
83. Aston-Jones G, Rajkowski J, Cohen J. Role of locus coeruleus in attention and behavioral flexibility. Biol Psychiatry. 1999;46:1309–20.
84. Uematsu A, Tan BZ, Johansen JP. Projection specificity in heterogeneous locus coeruleus cell populations: implications for learning and memory. Learn Mem. 2015;22:444–51.
85. Kawaguchi Y, Shindou T. Noradrenergic excitation and inhibition of GABAergic cell types in rat frontal cortex. J Neurosci. 1998;18:6963–76.
86. McCormick DA, Prince DA. Noradrenergic modulation of firing pattern in guinea pig and cat thalamic neurons, in vitro. J Neurophysiol. 1988;59:978–96.
87. Chiu CQ, Martenson JS, Yamazaki M, Natsume R, Sakimura K, Tomita S, et al. Input-specific NMDAR-dependent potentiation of dendritic GABAergic inhibition. Neuron. 2018;97:368–77. e3.
88. Kawaguchi Y, Kubota Y. GABAergic cell subtypes and their synaptic connections in rat frontal cortex. Cereb Cortex. 1997;7:476–86.
89. Mank M, Santos AF, Direnberger S, Mrsic-Flogel TD, Hofer SB, Stein V, et al. A genetically encoded calcium indicator for chronic in vivo two-photon imaging. Nat Methods. 2008;5:805–11.
90. Rose T, Jaepel J, Hubener M, Bonhoeffer T. Cell-specific restoration of stimulus preference after monocular deprivation in the visual cortex. Science. 2016;352:1319–22.
91. Tolias AS, Ecker AS, Siapas AG, Hoenselaar A, Keliris GA, Logothetis NK. Recording chronically from the same neurons in awake, behaving primates. J Neurophysiol. 2007;98:3780–90.
92. Margolis DJ, Lutcke H, Schulz K, Haiss F, Weber B, Kugler S, et al. Reorganization of cortical population activity imaged throughout long-term sensory deprivation. Nat Neurosci. 2012;15:1539–46.
93. Chestek CA, Batista AP, Santhanam G, Yu BM, Afshar A, Cunningham JP, et al. Single-neuron stability during repeated reaching in macaque premotor cortex. J Neurosci. 2007;27:10742–50.
94. Ganguly K, Carmena JM. Emergence of a stable cortical map for neuroprosthetic control. PLoS Biol. 2009;7:e1000153.
95. Peters AJ, Chen SX, Komiyama T. Emergence of reproducible spatiotemporal activity during motor learning. Nature. 2014;510:263–7.
96. Stevenson IH, Cherian A, London BM, Sachs NA, Lindberg E, Reimer J, et al. Statistical assessment of the stability of neural movement representations. J Neurophysiol. 2011;106:764–74.
97. Kentros CG, Agnihotri NT, Streater S, Hawkins RD, Kandel ER. Increased attention to spatial context increases both place field stability and spatial memory. Neuron. 2004;42:283–95.
98. Ziv Y, Burns LD, Cocker ED, Hamel EO, Ghosh KK, Kitch LJ, et al. Long-term dynamics of CA1 hippocampal place codes. Nat Neurosci. 2013;16:264–6.
99. Rao-Ruiz P, Visser E, Mitric M, Smit AB, van den Oever MC. A Synaptic Framework for the Persistence of Memory Engrams. Front Synaptic Neurosci. 2021;13:661476.
100. Rokni U, Richardson AG, Bizzi E, Seung HS. Motor learning with unstable neural representations. Neuron. 2007;54:653–66.
101. Mau W, Hasselmo ME, Cai DJ The brain in motion: How ensemble fluidity drives memory-updating and flexibility. Elife. 2020;9.
102. Cruz-Martin A, Crespo M, Portera-Cailliau C. Delayed stabilization of dendritic spines in fragile X mice. J Neurosci. 2010;30:7793–803.
103. Cruz-Martin A, Crespo M, Portera-Cailliau C. Glutamate induces the elongation of early dendritic protrusions via mGluRs in wild type mice, but not in fragile X mice. PLoS One. 2012;7:e32446.
104. Mostany R, Anstey JE, Crump KL, Maco B, Knott G, Portera-Cailliau C. Altered synaptic dynamics during normal brain aging. J Neurosci. 2013;33:4094–104.

ACKNOWLEDGEMENTS

We thank all members in the Cruz-Martín lab, as well as Margaret Minnig, Timothy Otchy, Nathan Perkins, and Daniel P. Leman for optimization of miniscope imaging and lens implant placement, Tim Gardner for providing access to 3D printers and sharing video acquisition software, Peyman Golshani and Daniel Aharoni for donating the camera sensor and data acquisition board for miniscope experiments. Ashley Comer, Nancy Padilla, Mark Howe, William A. Liberti 3rd, Michael Hasselmo, Camron Bryant, Renata Batista-Brito, Geoffrey Goodhill and members of the Cruz-Martín lab helped critically by reading the manuscript and engaging in helpful discussions. Todd Blute and the Boston University Biology Imaging Core provided use of the epifluorescence microscope. Lastly, we used the Boston University Shared Computing Cluster to analyze our data. This work was supported by a NARSAD Young Investigator Grant (AC-M, #27202), the NSF NRT UtB: Neurophotonics National Research Fellowship (LNK, #DGE-1633516), and the Boston University Undergraduate Research Opportunities Program (TPHN, WWY). The funders had no role in study design, data collection and analysis, decision to publish, or preparation of the manuscript.

AUTHOR CONTRIBUTIONS

CJ: Conceptualization: formulated ideas for data analysis (equal), formulated composition and goals of the experiments and paper (equal), Software: code writing and analysis for behavioral and Ca^{2+}imaging data (lead). Formal Analysis: analysis of behavioral and Ca^{2+} data, statistical analyses (lead). Investigation: surgeries, histology, episcope imaging, rabies cell counting (equal). Validation: validation of Ca^{2+}analysis strategy (equal). Writing—Original Draft: part of methods (support). Writing—Review & Editing: provided edits (equal). Visualization: figure generation (equal). LNK: Conceptualization: formulated composition and goals of the experiments and paper (equal), Software: behavioral analysis with DeepLabCut (equal). Formal Analysis: analysis of behavior, histology, trans-synaptic tracing, c-Fos data, and statistical analyses (equal). Investigation: surgeries and baseplating, behavioral experiments with and without miniscopes, histology, episcope imaging, rabies and c-Fos cell counting (lead). Validation: repeated miniscope experiments with new cohorts (equal). Writing—Original Draft: wrote initial draft (excluding part of methods and discussion) (lead). Writing—Review & Editing: re-wrote draft for revisions and incorporated edits (lead). Visualization: figure generation (equal). WWY Conceptualization: formulated composition and goals of the experiments and paper (equal), Methodology: miniscope adaptation design and construction, developed protocols for GRIN lens implant surgeries (lead). Investigation: surgeries and baseplating, behavioral experiments with miniscopes (equal). Writing—Review & Editing: provided edits (support). Visualization: figure generation (support). KKW Software: behavioral analysis with DeepLabCut (support). Investigation: surgeries, behavioral experiments without miniscopes, immunohistochemistry, histology, episcope imaging, rabies and c-Fos cell counting (equal). **BS:** Conceptualization: provided ideas for analysis (support). Investigation: set up DeepLabCut with our data (support). Supervision: oversight of some analysis projects (support). Writing—Review & Editing: provided edits (support). **AO'C:** Software: code writing and analysis of the output of DeepLabCut data (equal). RSL: Software: code writing for Ca^{2+} imaging analysis (support). Writing—Original Draft: part of methods (support). Visualization: activity heatmaps figure generation (support). JCJ: Methodology: taught us to perform surgeries and use miniscopes (equal). Writing—Review & Editing: provided edits (equal). RAP: Formal Analysis: analysis of behavioral and Ca^{2+} data (support). Investigation: rabies cell counting and layer quantification (support). **CY:** Investigation: annotation for behavioral analysis in DeepLabCut, histology, episcope imaging, rabies cell counting (support). TJJ: Formal Analysis: quantification of trans-synaptic tracing data (support). Investigation: surgeries, histology, immunohistochemistry, episcope imaging, cell counting (support). Writing—Review & Editing: provided edits (support). Visualization: figure generation (support). TPHN: Methodology: miniscope adaptation design and construction (equal). ESC: Investigation: annotation for behavioral analysis in DeepLabCut (support). EF: Investigation: surgeries, histology, episcope imaging, rabies cell counting (support). EDS: Investigation: histology, episcope imaging, rabies cell counting (support). BEV: Investigation: rabies cell counting (support). Writing—Review & Editing: provided edits (support). FSH: Investigation: perfusions and histology (support). LAF: Investigation: rabies cell counting and layer quantification (support). Writing—Review & Editing: provided edits (support). **AB:** Investigation: rabies cell counting (support). SM: Formal Analysis: electrophysiology data analysis (support). Investigation: ex vivo electrophysiology and optogenetic experiments (support). Visualization: figure generation (support). Writing—Review & Editing: feedback for original and revised draft (support). AC-M: Conceptualization: formulated composition, goals, and scope of the paper and approaches for analyses (lead), Formal Analysis: statistical analyses (equal). Writing—Original Draft: wrote some of discussion (equal). Writing—Review & Editing: editing and feedback for original and revised draft (equal). Visualization: figure design and generation (lead). Supervision: mentorship and oversight of the project (lead). Project Administration: management and coordination (lead). Funding acquisition (lead).

COMPETING INTERESTS

The authors declare no competing interests.

ADDITIONAL INFORMATION

Supplementary information The online version contains supplementary material available at https://doi.org/10.1038/s41380-022-01485-y.

Correspondence and requests for materials should be addressed to Alberto Cruz-Martín.